Biallelic Mutations in Nuclear Pore Complex Subunit *NUP107* Cause Early-Childhood-Onset Steroid-Resistant Nephrotic Syndrome

Noriko Miyake,[1,17] Hiroyasu Tsukaguchi,[2,17,*] Eriko Koshimizu,[1] Akemi Shono,[3] Satoko Matsunaga,[4] Masaaki Shiina,[5] Yasuhiro Mimura,[6] Shintaro Imamura,[7] Tomonori Hirose,[8] Koji Okudela,[9] Kandai Nozu,[3] Yuko Akioka,[10] Motoshi Hattori,[10] Norishige Yoshikawa,[11] Akiko Kitamura,[12] Hae Il Cheong,[13,14,15] Shoji Kagami,[16] Michiaki Yamashita,[7] Atsushi Fujita,[1] Satoko Miyatake,[1] Yoshinori Tsurusaki,[1] Mitsuko Nakashima,[1] Hirotomo Saitsu,[1] Kenichi Ohashi,[9] Naoko Imamoto,[6] Akihide Ryo,[4] Kazuhiro Ogata,[5] Kazumoto Iijima,[3] and Naomichi Matsumoto[1,*]

The nuclear pore complex (NPC) is a huge protein complex embedded in the nuclear envelope. It has central functions in nucleocytoplasmic transport, nuclear framework, and gene regulation. Nucleoporin 107 kDa (NUP107) is a component of the NPC central scaffold and is an essential protein in all eukaryotic cells. Here, we report on biallelic *NUP107* mutations in nine affected individuals who are from five unrelated families and show early-onset steroid-resistant nephrotic syndrome (SRNS). These individuals have pathologically focal segmental glomerulosclerosis, a condition that leads to end-stage renal disease with high frequency. *NUP107* is ubiquitously expressed, including in glomerular podocytes. Three of four *NUP107* mutations detected in the affected individuals hamper NUP107 binding to NUP133 (nucleoporin 133 kDa) and NUP107 incorporation into NPCs in vitro. Zebrafish with *nup107* knockdown generated by morpholino oligonucleotides displayed hypoplastic glomerulus structures and abnormal podocyte foot processes, thereby mimicking the pathological changes seen in the kidneys of the SRNS individuals with *NUP107* mutations. Considering the unique properties of the podocyte (highly differentiated foot-process architecture and slit membrane and the inability to regenerate), we propose a "podocyte-injury model" as the pathomechanism for SRNS due to biallelic *NUP107* mutations.

Introduction

Nephrotic syndrome (NS) is a renal disease caused by disruption of the glomerular filtration barrier, which results in massive proteinuria, hypoalbuminemia, and dyslipidemia. Idiopathic NS occurs in 16/100,000 children.[1] Most children with idiopathic NS respond well to steroids, but 10%–20% of affected children are categorized as having steroid-resistant NS (SRNS).[2–6] SRNS is a clinically and genetically heterogeneous renal disorder that might have an immunological, structural, or functional etiology.[2,5,7–9] Higher rates of genetic delineation are expected in early-onset SRNS.[7] Clinical differences in SRNS have been suggested to depend on its age of onset.[7] Current medical management and prognosis in NS are based largely on the histological diagnosis. Effective SRNS treatments are not well established, and renal transplantation is eventually required. Importantly, 63%–73% of those with childhood-onset SRNS show pathologically focal segmental glomerulosclerosis (FSGS),which carries a great risk of progression to end-stage renal disease (ESRD).[1,6,8,10] To date, at least 27 genes are associated with SRNS, thereby expanding our knowledge of the pathomechanisms involved in SRNS and podocyte development and function.[11] Although SRNS is the leading cause of ESRD in children worldwide, approximately 70% of those with childhood-onset SRNS are genetically uncharacterized.[7,11] We describe here an additional genetic cause of early-onset SRNS and propose its possible pathomechanism.

Material and Methods

Human Subjects

A total of 18 families (10 with affected siblings and 8 with a single affected individual) who lack any known genetic causes of SRNS (in 27 known genes) were recruited to this study. They presented with non-syndromic early-onset SRNS with onset ages between 1 and 11 years. The clinical aspects of 7 of the 18 families have

[1]Department of Human Genetics, Yokohama City University Graduate School of Medicine, Yokohama 236-0004, Japan; [2]Second Department of Internal Medicine, Kansai Medical University, Osaka 570-8507, Japan; [3]Department of Pediatrics, Kobe University Graduate School of Medicine, Kobe 650-0017, Japan; [4]Department of Microbiology, Yokohama City University Graduate School of Medicine, Yokohama 236-0004, Japan; [5]Department of Biochemistry, Yokohama City University Graduate School of Medicine, Yokohama 236-0004, Japan; [6]Cellular Dynamics Laboratory, RIKEN, Wako 351-0198, Japan; [7]National Research Institute of Fisheries Science, Yokohama 236-8648, Japan; [8]Department of Molecular Biology, Yokohama City University Graduate School of Medicine, Yokohama 236-0004, Japan; [9]Department of Pathology, Yokohama City University Graduate School of Medicine, Yokohama 236-0004, Japan; [10]Department of Pediatric Nephrology, Tokyo Women's Medical University, Tokyo 162-8666, Japan; [11]Center for Clinical Research and Development, National Center for Child Health and Development, Tokyo 157-8535, Japan; [12]Department of Immunology & Parasitology, Institute of Biomedical Sciences, Tokushima University Graduate School, Tokushima 770-8503, Japan; [13]Department of Pediatrics, Seoul National University Children's Hospital, Seoul 03080, Korea; [14]Research Coordination Center for Rare Diseases, Seoul National University Hospital, Seoul 03080, Korea; [15]Kidney Research Institute, Medical Research Center, Seoul National University College of Medicine, Seoul 03080, Korea; [16]Department of Pediatrics, University of Tokushima Graduate School, Tokushima 770-8503, Japan
[17]These authors contributed equally to this work
*Correspondence: tsukaguh@hirakata.kmu.ac.jp (H.T.), naomat@yokohama-cu.ac.jp (N.M.)
http://dx.doi.org/10.1016/j.ajhg.2015.08.013.

been described previously.[12] Affected individuals were resistant to standard steroid therapy but were partially responsive to immunosuppressive drugs. At least ten affected individuals in eight families underwent renal transplants and have had no recurrence of SRNS to date. All samples were collected after written informed consent was obtained. The study protocol was approved by the institutional review boards of Yokohama City University School of Medicine, Kansai Medical University, RIKEN, Tokyo Women's Hospital, and Kobe University.

DNA Extraction

Peripheral-blood leukocytes or saliva from affected individuals and their families was collected. Genomic DNA was extracted with a QIAamp DNA Blood Max Kit (QIAGEN) or Oragene DNA (DNA Genoteck) according to the instructions of each manufacturer.

Whole-Exome Sequencing and Informatics Analyses

Whole-exome sequencing (WES) was performed on affected individuals (one individual from each family) and their parents when the samples were available, as reported previously.[13] In brief, 3-μg samples of genomic DNA were sheared with the Covaris S2 system (Covaris); genome partitioning was performed with SureSelect Human All Exon V5 (Agilent Technology) according to the manufacturer's instructions. Prepared samples were run on a HiSeq 2000 instrument (Illumina) with 101-bp paired-end reads and 7-bp index reads. The sequence reads were mapped to the human reference sequence (GRCh37) by Novoalign 3.00. Next, PCR duplication and variant calls were processed by Picard and the Genome Analysis Toolkit. Ten of the 18 families have multiple affected children, suggesting the autosomal-recessive model, in which homozygous or compound-heterozygous variants are focused in each affected individual. Genetic variants in exons and canonical splice sites (±2 bp) with a minor allele frequency (MAF) of >0.005 in the NHLBI Exome Sequencing Project Exome Variant Server (EVS), Exome Aggregation Consortium (ExAC) Browser, Human Genetic Variation Database (HGVD, which is a public exome database for the Japanese population), or in-house Japanese exome data (n = 575) were removed from the candidates. Genes that harbor recessive variants detected commonly in two or more probands were selected. Candidate recessive variants were checked in each family by Sanger sequencing for confirmation that such variants co-segregated with the disease.

Haplotype Analysis

To determine the haplotype associated with c.2492A>C (p.Asp831Ala), which was found commonly in the five families, we amplified samples of genomic DNA or whole-genome-amplified DNA with 13 microsatellite markers (*D12S364*, *S12S310*, *D12S1617*, *D12S345*, *D12S85*, *D12S368*, *D12S83*, *D12S326*, *D12S351*, *D12S346*, *D12S78*, *D12S79*, and *D12S86*) from the ABI PRISM Linkage Mapping Set (Life Technologies).The PCR products were run on a 3500xl Genetic Analyzer (Life Technologies) and analyzed with GeneMapper 5 software (Life Technologies). Additionally, informative SNPs were chosen from the WES data for each affected individual and used thereafter for constructing haplotype blocks.

Expression of Human *NUP107*

NUP107 (nucleoporin 107 kDa; GenBank: NM_020401.2; MIM: 607617) expression in human embryos and adults was checked by a TaqMan Gene Expression Assay with two probe sets (Hs00914854_g1 and Hs00220703_m1 from Life Technologies) internally standardized by beta actin (Life Technologies). cDNA from human fetal and adult tissues was purchased from Clontech. qPCR was performed by a Rotor-Gene Q instrument (QIAGEN), the data from which was analyzed by the ΔΔCt method with Rotor-Gene 6000 Series software (QIAGEN). The experiments were done in duplicate. The expression level of each tissue represents the mean value of the duplicates.

Histopathology and Transmission Electron Microscopy on Samples from Individuals with Early-Onset SRNS

We stained 3-μm-thick sections cut from paraffin-embedded biopsied kidney tissues with H&E, periodic acid-Schiff stain, and periodic acid methenamine silver stain according to standard methods. For transmission electron microscopy, 1-mm renal-biopsy specimen cubes were fixed in 2% phosphate-buffered glutaraldehyde (pH 7.3) at room temperature, dehydrated in an alcohol gradient, and embedded in Epon-Araldite resin. Sections of 1-μm thickness were cut with an ultra-microtome (Ultracut UCT, Leica), stained with toluidine blue, and examined with a light microscope. Ultrathin sections (60–90 nm) stained by lead citrate were examined with a JEM1011 transmission electron microscope (JEOL). The TUNEL method was used to detect apoptotic cells on tissue sections with an in situ apoptosis detection kit (Takara) according to the manufacturer's instruction.

Immunofluorescence Microscopy

We deparaffinized and rehydrated 3-μm-thick paraffin sections of a necropsy specimen and then autoclaved them in target retrieval solution (S1700, Dako) for 15 min at 105°C. The sections were subjected to immunofluorescence labeling with primary antibodies including rabbit anti-NUP107 mAb (1.5 μg/ml, EPR12241, ab182559, Abcam), mouse anti-WT1 mAb (1:100, WT49, NCL-L-WT1-562, Leica), and mouse anti-Ezrin mAb (1:500, 3C12, E8897, lot 102K4824, Sigma-Aldrich). Normal rabbit and mouse immunoglobulins (IgGs) (sc-2027 [lot L1212] and sc-2025 [lot H1512], respectively, Santa Cruz) were used for negative controls. The CSAII kit (K1497, DAKO) was used for signal amplification of WT1, and other primary antibodies were visualized with Alexa555-conjugated anti-rabbit (1 μg/ml) or Alexa647-conjugated anti-mouse IgG (2 μg/ml) secondary antibodies (A21429 or A21236, respectively, Life Technologies), and then samples were mounted with ProLong Gold antifade reagent (P36930, Life Technologies). Single optical sections were acquired at 16-bit data depth with a confocal microscope system (AxioImager.Z1 microscope with LSM 700 laser scanner, Carl Zeiss) equipped with a C-Apochromat water immersion objective (40×, 1.2 numerical aperture [NA], Carl Zeiss); images were arranged with Photoshop CS5 (Adobe Systems).

Expression Vectors

Mammalian expression vectors were prepared with the Gateway system (Life Technologies). The *NUP107* open reading frame was amplified by PCR with human cDNA derived from a human lymphoblastoid cell line. The PCR product was introduced into the Gateway pDONR221 vector (Life Technologies), and its sequence was confirmed by Sanger sequencing. For mutagenesis, a QuickChange II XL Site-Directed Mutagenesis Kit (Agilent Technologies) was used. After confirming appropriate mutagenesis, we performed LR recombination to create a mammalian expression

vector (pcDNA-DEST53, Life Technologies) to produce N-terminally GFP-fused NUP107 proteins. Among four *NUP107* mutations observed in this cohort, c.969+1G>A was mimicked by c.969_970insTAG, which created the nonsense codon just after the mutation (p.Asp324*). Whereas two truncating mutations (c.969+1G>A and c.1079_1083delAAGAG [p.Glu360Glyfs*6]) are thought unlikely to be present in vivo because of nonsense-mediated decay, these constructs were used as controls for the binding loss, given that C-terminally truncated proteins reportedly lose the NUP107-NUP133 interaction.[14]

Cell-free Protein Synthesis and In Vitro Pull-Down Assays

In vitro transcription and cell-free protein synthesis were performed as described previously.[15,16] In vitro transcription templates for wild-type or mutant *NUP107* were amplified by slit-primer PCR. For generation of transcription templates, the first PCR was performed with 50 ng/μl of each plasmid, 100 nM of the S1 common primer (5′-CCACCCACCACCACCAACAAAAAAG CAGGCTATG-3′), and 100 nM of the vector-specific reverse primer (5′-ATCTTTTCTACGGGGTCTGA-3′). The second PCR was performed with the first PCR product as a template with 100 μM of the SPu primer (5′-GCGTAGCATTTAGGTGACACT-3′), 100 μM of the vector-specific reverse primer (5′-ACGTTAAGGGATTTTGGT CA-3′), and 1 μM of either the deSP6-E02-FLAG-tagged primer or the biotin-ligation site (bls) primer for the addition of the nucleotide sequences of the FLAG tag or the bls tag, respectively (FLAG tagged: 5′-GGTGACACTATAGAACTCACCTATCTCTCTACACAAA ACATTTCCCTACATACAACTTTCAACTTCCTATTATGGACTACAA GGATGACGATGACAAGCTCCACCCACCACCACCAATG-3′; bls tagged: 5′-GGTGACACTATAGAACTCACCTATCTCTCTACACAAA ACATTTCCCTACATACAACTTTCAACTTCCTATTATGGGCCTGA ACGACATCTTCGAGGCCCAGAAGATCGAGTGGCACGAACTCC ACCCACCACCACCAATG-3′).

An ENDEXT Wheat Germ Expression Kit (CellFree Sciences) was used for cell-free protein synthesis according to the manufacturer's instructions for the bilayer translation method. Biotinylated proteins were produced as described previously.[17]

Biotinylated wild-type or altered NUP107 was mixed with FLAG-NUP133 (nucleoporin 133 kDa; GenBank: NM_018230.2; MIM: 607613) in lysis buffer containing 25 mM Tris-HCl (pH 7.5), 100 mM NaCl, 1 mM EDTA, 2% Triton X-100, 1 mM DTT, and 10 mg/ml BSA. After incubation for 1 hr at 26°C, streptavidin MagneSphere beads (Promega) were added, and the mixture was incubated for 30 min at room temperature. After three washes with lysis buffer, bound proteins were eluted from the beads with 20 μl of 2× SDS sample buffer. Bound proteins were separated by SDS-PAGE followed by immunoblotting with an anti-FLAG antibody (Sigma-Aldrich) or a Streptavidin-HRP conjugate (GE Healthcare). Proteins on the blot were detected with Immobilon Western Chemiluminescent HRP Substrate (Millipore) and FluorChem FC2 (Alpha Innotech) in accordance with the protocol from each manufacturer.

Immunoprecipitation

The cell lysate used for immunoprecipitation was prepared according to a method reported previously[18,19] with a slight modification. In brief, HeLa cells were transfected with the wild-type or altered N-terminally GFP-fused NUP107 construct by Viafect (Promega) according to the manufacturer's instructions. The cells were lysed with lysis buffer containing 10 mM Tris-HCl (pH 7.4), 400 mM NaCl, 1% Triton X-100, 2 mM EDTA, 1 mM DTT supplemented with complete proteinase inhibitor cocktail (Roche Diagnostics GmbH), and PhosSTOP (Roche Diagnostics); sonicated; and then incubated for 30 min at 4°C. For debris removal, the crude lysate was centrifuged at 20,630 × *g* for 20 min at 4°C. After collection, the supernatant was diluted 3.75× in dilution buffer (10 mM Tris-HCl [pH 7.4], 2 mM EDTA, 1 mM DTT, complete proteinase inhibitor cocktail, and PhosSTOP). For immunoprecipitation of the GFP-fused NUP107, mouse anti-GFP antibody (11-814-460-001, Roche Diagnostics) and Protein G Sepharose beads (17-0618-01, GE Healthcare) were added. After incubation for 2 hr at 4°C, the beads were washed with wash buffer (lysis buffer diluted 3.75× in dilution buffer). After the protein-bound beads were boiled, they were run on an SDS-PAGE gel and transferred to a polyvinylidene fluoride membrane (Millipore). Membranes prepared in this manner were incubated in 0.2% Casein in Tris-buffered saline containing 0.1% Tween 20 (TBS-T) for blocking. The membrane was probed with rabbit anti-GFP primary antibody (598, MBL) diluted at 1:1,000 and mouse anti-NUP133 (M00055746-M01, Abnova) diluted at 1:500 followed by secondary antibodies HRP-rabbit anti-rat IgG (A5795, Sigma-Aldrich) and HRP-goat anti-mouse IgG (170-6516, Bio-Rad) both diluted at 1:3,000 with 0.2% Casein in TBS-T. For obtaining protein signals, Immobilon Western Chemiluminescent HRP Substrate (Millipore) was used as a chemiluminescence substrate.

Subcellular Localization of NUP107

HeLa cells cultured in DMEM (Life Technologies) containing 10% fetal bovine serum (Sigma-Aldrich) at 37°C in an atmosphere of 5% CO_2 on poly-L-lysine-coated coverslips (Wako) were transfected with the wild-type or altered N-terminally GFP-fused NUP107 vector with the use of Viafect (Promega). After incubation for 48 hr, the cells were washed with pre-warmed PBS at 37°C and then fixed with pre-warmed 2% paraformaldehyde (Wako) in PBS at 37°C for 10 min. The cells were treated with 0.5% Triton X-100 in PBS for 2.5 min and then incubated with 5% normal goat serum (NGS, Merck Millipore) in PBS for 1 hr. After blocking, the cells were reacted with the primary antibody (MAb414 [mouse anti-nuclear pore complex (NPC) proteins], MMS-120P, Covance) diluted at 1:3,000 in 1% NGS in PBS for 2 hr, washed with PBS, and then reacted with the secondary antibody (Alexa Fluor 594 goat anti-mouse IgG, A11032, Life Technologies) in 1% NGS in PBS for 2 hr. After staining, the cells were mounted in paraphenylenediamine solution (80% glycerol in PBS and 1 mg/ml paraphenylenediamine, 11873580001, Roche Diagnostics). Images were captured with a DeltaVision microscope (Applied Precision) equipped with a Plan Apo objective lens (100×, 1.35 NA, Olympus) and a Cool Snap HQ2 CCD camera (Photometrics).

Zebrafish Knockdown by Microinjection of Morpholino Oligonucleotides

The antisense morpholino oligonucleotides (MOs) for *nup107* translation blocking (TB) (5′-AAGTCTGACTCCATTCCATATT GTC-3′)[20] and for *nup107* splice blocking (SB) (5′-ATACATTTA AGCTCACCTCTCTGAC-3′) and a standard MO control (5′-CCT CTTACCTCAGTTACAATTTATA-3′) obtained from Gene Tools were injected into 1- to 2-cell-stage embryos, each at a final concentration of 0.25 mM. The experiment was authorized by the Institutional Committee for Fish Experiments at the National Research Institute of Fisheries Science.

RNA Isolation and RT-PCR Analysis

Total RNA was extracted from embryos at 24 hr post-fertilization (hpf) with TRIzol reagent according to the manufacturer's (Life Technologies) protocol. Double-stranded cDNA was synthesized with M-MLV reverse transcriptase (Promega) and then amplified by PCR with ExTaq (Takara). For detecting the splicing mutation (caused by the MO injections) in *nup107* exon 24, the following primers were used: 5′-TGAACTGTCCTCCGGTGAAG-3′ (forward) and 5′-TGCGATGATGTCAGCAAGAC-3′ (reverse). For the PCR amplifications, the initial denaturing step at 94°C for 5 min was followed by 29 cycles of 30 s at 94°C, 30 s at 61°C, 30 s at 72°C, and a final extension of 7 min at 72°C. PCR products were separated on 3% agarose gels.

Histopathology and Transmission Electron Microscopy of Zebrafish

Larvae injected with control MO, *nup107*-TB MO, and *nup107*-SB MO at 5.5 days after fertilization were fixed with 2% paraformaldehyde and 2% glutaraldehyde in 0.1 M cacodylate buffer (pH 7.4) at 4°C overnight. After fixation, the samples were washed three times with 0.1 M cacodylate buffer for 30 min each and then postfixed with 2% osmium tetroxide in 0.1 M cacodylate buffer at 4°C for 3 hr. The samples were dehydrated in graded ethanol solution (50%, 70%, 90%, and 100%), infiltrated with propylene oxide (PO) two times for 30 min each, immersed in a 70:30 mixture of PO and resin (Quetol-812, Nisshin EM) for 1 hr, and then kept in an open-capped tube so that volatile PO would evaporate overnight. The samples were transferred to fresh 100% resin and polymerized at 60°C for 48 hr. The polymerized resins were cut into semi-thin (1.5-μm) sections with an Ultracut UCT (Leica) and then stained with 0.5% toluidine blue. Ultra-thin (70-nm) sections were cut on an Ultracut UCT (Leica) ultramicrotome and mounted on copper grids. The sections were stained with 2% uranyl acetate at room temperature for 15 min, washed with distilled water, and stained with lead stain solution (Sigma-Aldrich) at room temperature for 3 min. The grids were observed with a transmission electron microscope (JEM-1400Plus, JEOL) at 80 kV.

Molecular-Dynamics Simulation of the p.Asp831Ala Substitution in NUP107

Molecular-dynamics (MD) simulations of the wild-type and p.Asp831Ala Nup107 were carried out with the program package GROMACS (Groningen Machine for Chemical Simulation) version 5.0 with the Optimized Potentials for Liquid Simulations all-atom force field based on the local Møller-Plesset perturbation theory (OPLS-AA/L).[21] The starting structure of NUP107 was extracted from the crystal structure of the NUP107-NUP133 complex (PDB: 3CQC). The missing regions in NUP107 were modeled with the Phyre2 modeling server,[22] and the p.Asp831Ala substitution was introduced with FoldX software.[23] The wild-type and altered NUP107 molecules were solvated with simple-point-charge water molecules in a cubic box extending at least 1.0 nm from the protein surface. Sodium ions were added to neutralize the systems, which were then subjected to energy minimization for 50,000 steps by steepest descent. The minimized systems were then equilibrated by position-restrained MD simulation for soaking the water molecules in the macromolecules in two steps as follows: an NVT ensemble (constant number of particles, volume, and temperature) for 100 ps and an NPT ensemble (constant number of particles, pressure, and temperature) for 4,000 ps each at 310 K. The well-equilibrated systems were then subjected to MD simulations for 30 ns each at 310 K without any restrictions. In all simulations, for maintaining a constant temperature of 310 K, temperature coupling using velocity rescaling with a stochastic term[24] was employed with a coupling constant τ of 0.1 ps. Van der Waals interactions were modeled with 6–12 Lennard-Jones potentials with a 1.4-nm cutoff. Long-range electrostatic interactions were calculated with the particle-mesh Ewald method[25] with a 1.4-nm cutoff for the real-space term. Covalent bonds were constrained with the LINCS algorithm.[26]

Results

Pathogenic Mutations Detected by WES

To identify the genetic cause of early-onset SRNS, we performed WES on 18 probands. Because we found multiple affected siblings in ten families, we speculated on an autosomal-recessive inheritance pattern for SRNS and focused on the recessive variants shared by two or more families with well-performed WES data (Tables S1–S3, S4, and S5). Biallelic mutations in *NUP107*, which encodes NUP107, were common in five families, and the mutation co-segregated perfectly with the affected state in all five families (Figure 1A, Table 1, and Figure S1). None of the other families in our cohort had any pathological variants in *NUP107* or any other known genes associated with SRNS, as listed in Table S6.

We identified a total of four *NUP107* mutations, including two missense mutations (c.469G>T [p.Asp157Tyr] and c.2492A>C [p.Asp831Ala]), one 5-bp deletion (c.1079_1083delAAGAG [p.Glu360Glyfs*6]), and one splice-donor-site mutation (c.969+1G>A) (Table 2). Heterozygous c.2492A>C was common in all five families. The two missense mutations altered evolutionally conserved amino acids (Figure S2) and were predicted to be pathogenic by web-based programs PolyPhen-2 and MutationTaster (Table 2). Furthermore, p.Asp831Ala resides within the Nup84-Nup100 domain (Figure S3). The 5-bp deletion was subjected to nonsense-mediated mRNA decay and probably led to a lack of protein synthesis (Figure S4). The splicing mutation (c.969+1G>A) causes a loss of the intrinsic splicing donor site (Figure S5). All four variants were examined in the EVS, ExAC Browser, HGVD, and in-house Japanese exome database (n = 575). The c.1079_1083delAAGAG variant was observed at frequencies of 0.0000083 in the ExAC Browser and 0.0008696 in the in-house Japanese exome data. Another variant, c.2492A>C, was observed at a frequency of 0.0013587 only in HGVD, but not in the EVS, ExAC Browser, or in-house Japanese exome data (Table 2). The other mutations (c.469G>T and c.969+1G>A) were never observed in any of four variant databases. Among 881 *NUP107* variants registered in the ExAC Browser, a total of 31 variants with a MAF $\geq$ 0.005 were in non-coding regions (intronic but not in canonical acceptor or donor sites or UTRs) or were synonymous variants (Table S7). Furthermore, 36 loss-of-function variants in *NUP107* are not homozygous (all heterozygous; Table S8). Therefore, this genetic

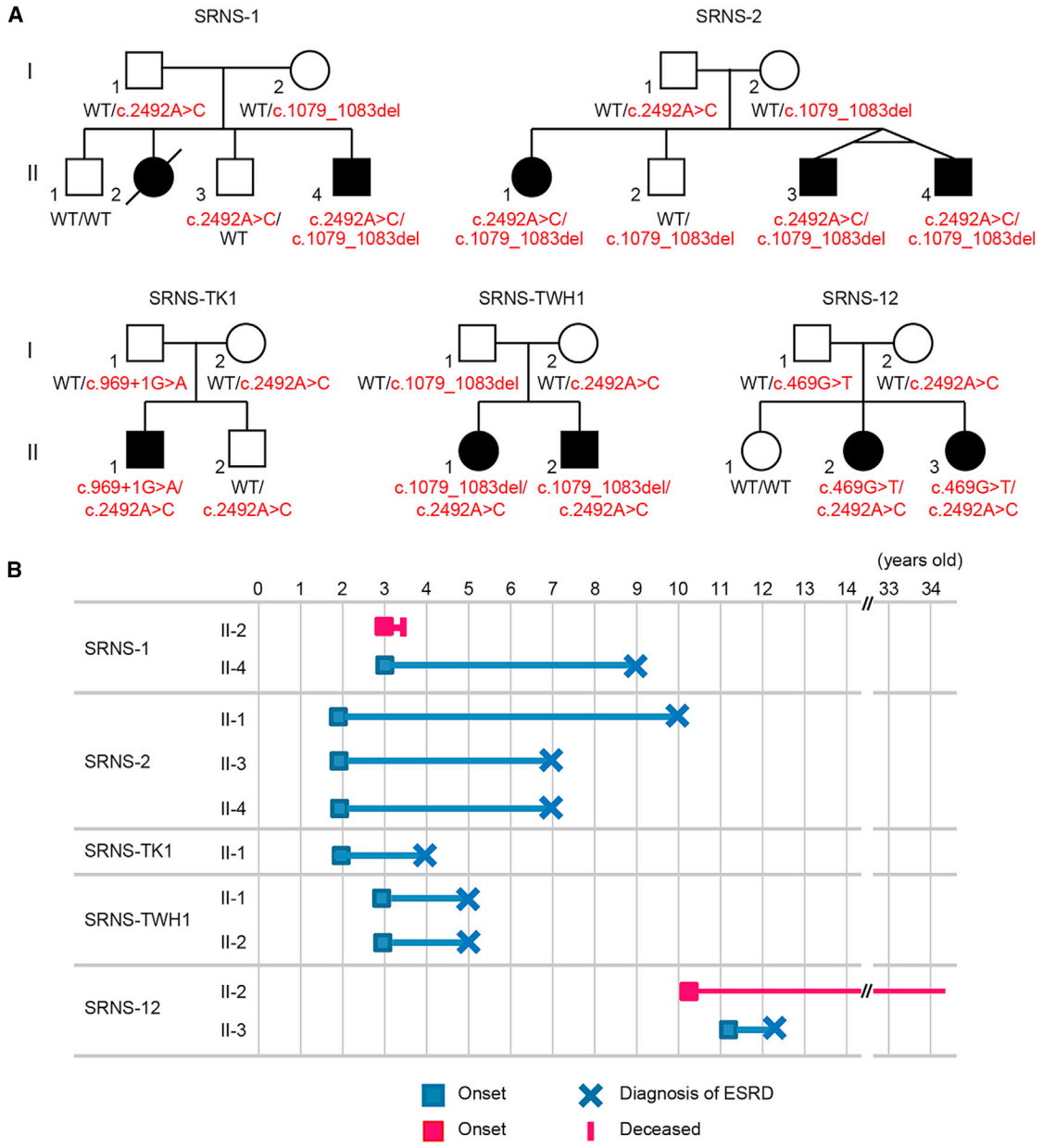

Figure 1. Genetic Analysis and Clinical Course of Early-Onset SRNS in Affected Individuals with *NUP107* Mutations
(A) Familial pedigrees and *NUP107* mutations. Mutant alleles are colored in red. WT indicates the wild-type allele. Filled and unfilled symbols represent affected and unaffected members, respectively.
(B) Clinical course of the affected individuals. The onset of renal symptoms and diagnosis of ESRD are represented by squares and crosses, respectively. Blue and red horizontal bars indicate the period leading to ESRD and the period before completed ESRD, respectively. SRNS-1 II-2 died from a viral infection before the advent of ESRD.

evidence strongly suggests that biallelic *NUP107* mutations could lead to autosomal-recessive SRNS.

A Common Haplotype Harboring c.2492A>C

Interestingly, all affected individuals carry c.2492A>C heterozygously. To determine whether c.2492A>C was derived from an ancestral chromosome, we constructed the haplotype in all families by using informative microsatellite markers and SNPs. We confirmed that a 412-kb haplotype was shared by all five families (Figure S6). Considering the extreme rarity of c.2492A>C in different whole-exome databases, c.2492A>C is likely to be specific to East Asians.

Clinical Characterization of NUP107-Related SRNS

Noticeably, the clinical course of affected individuals with *NUP107* mutations was similar (Figure 1B and the supplemental note). In brief, the four families consistently showed early-onset SRNS whereby NS first manifested itself at age 2–3 years and ESRD became evident before age 10

Table 1. Clinical and Genetic Summary of SRNS-Affected Families Harboring *NUP107* Mutations

Family	Individual	Mutation	Age at Onset (Years)	Age at Diagnosis of ESRD (Years)	Treatment	Histology (Subtype, Age in Years)
SRNS-1[a]	II-2[b]	ND	3	NA	Pred	FSGS (NOS, 3)
	II-4	c.[1079_1083del];[2492A>C]	3	9	Pred, CyA, CPA	FSGS (NOS, 3)
SRNS-2[a]	II-1	c.[1079_1083del];[2492A>C]	2	10	Pred, CPA	MCNS (NOS, 2), FSGS (NOS, 4)
	II-3	c.[1079_1083del];[2492A>C]	2	7	Pred	MCNS (2)
	II-4	c.[1079_1083del];[2492A>C]	2	7	Pred	FSGS (NOS, 2)
SRNS-TK1	II-1	c.[969+1G>A];[2492A>C]	2	4	Pred, CyA, CPA	FSGS (NOS, 2)
SRNS-TWH1	II-1	c.[1079_1083del];[2492A>C]	3	5	Pred, ARB, PP	FSGS (collapsing, 3)
	II-2	c.[1079_1083del];[2492A>C]	3	5	Pred, CyA, ARB	FSGS (collapsing, 3)
SRNS-12[a]	II-2	c.[469G>T];[2492A>C]	10	NA	ARB	ND
	II-3	c.[469G>T];[2492A>C]	11	12	Pred, ARB	FSGS (NOS, 11)

Abbreviations are as follows: ARB, AT II receptor blocker; collapsing, collapsing variants; CPA, cyclophosphamide; CyA, cyclosporine A; ESRD, end-stage renal disease; FSGS, focal segmental glomerulosclerosis; MCNS, minimal-change nephrotic syndrome; NA, not applicable; ND, not determined; NOS, non-specific type; PP, plasmapheresis; Pred, prednisone.
[a]These families appear in a previous report by Kitamura et al.[12]
[b]This individual died from a viral infection at the age of 3 years.

years. One family (SRNS-12) showed an exceptionally late onset of NS, which appeared after 10 years of age, and renal function has been relatively preserved at the current 34 years of age. Renal biopsies revealed histopathological FSGS in all affected individuals (Figure 2, Table 1, and Figure S7). Depletion of NUP107 was shown to lead to apoptosis in eukaryotes,[20,27] and we observed apoptotic changes in the renal biopsy samples from SRNS individuals (SRNS-TWH1 II-1 and II-2) with *NUP107* mutations. Cells with the characteristic morphological features, such as nuclear shrinkage and fragmentation, were occasionally found in the glomeruli and renal tubules (Figure S8). Some of these cells could be TUNEL positive (apoptotic), although we failed to recognize TUNEL-positive cells in the glomeruli of the few biopsied specimens, given that only ten glomeruli were observed (data not shown). Among them, five individuals underwent renal transplants and have experienced no recurrence of SRNS to date. Additionally, none of them showed neurological phenotypes.

NUP107 Function and *NUP107* Expression in Humans

NUP107 is an essential component of the NPC, which is one of the largest protein complexes (~125 MDa in vertebrates) in eukaryotes and comprises ~30 nucleoporins embedded in the nuclear envelope.[28,29] It facilitates the efficient transfer of macromolecules between the nucleus and cytoplasm in a highly selective manner and plays pivotal roles in the nuclear framework and gene expression.[28,30–33] Although some nucleoporins have tissue specificity,[34] *NUP107* and NUP107 are ubiquitously expressed as the core gene and the essential scaffold protein, respectively, of the NPC.[29,35–37] As the results of the TaqMan expression assay show, *NUP107* is expressed ubiquitously in most human fetal and adult tissues, including the kidney (Figure S9). To evaluate the physiological relevance of NUP107 in human podocytes, we examined the intracellular localization of NUP107, along with WT1 (a podocyte-specific transcription factor[38]) and Ezrin (a marker protein for apical domains of epithelial cells[39]), in human podocytes. Confocal microscopy demonstrated that NUP107 co-localized with WT1 and was distributed in a speckle-like pattern in the nuclei of human podocytes surrounding the glomerular capillary tufts (Figure S10). In addition to podocytes, most other cell types showed a similar staining pattern for NUP107. These data suggest that NUP107 has an important function for renal filtration in human podocytes. A direct link between NUP107 and renal disease has never been shown, but *NUP107* knockdown in HeLa cells altered the localization of ELYS, and this affected the proper localization of lamin A/C,[19] an alteration in which caused FSGS.[40]

Effect of the Common NUP107 p.Asp831Ala Substitution on the Structure of the Protein and Its Binding to NUP133

To evaluate the effect of p.Asp157Tyr and p.Asp831Ala substitutions from a structural viewpoint, we mapped the variant positions on the crystal structure of the yeast Sec13-Nup145C-Nup84 complex (PDB: 3IKO),[41] which is analogous to the human SEC13-NUP96-NUP107 complex (NUP96 is the C-terminal half product of *NUP98* [GenBank: NM_016320.4; MIM: 601021], processed after translation[42,43]) and the human NUP107-NUP133 complex (PDB: 3CQC).[14] Asp157 is predicted to reside on the surface of the protein, suggesting that the p.Asp157Tyr substitution does not affect the folded structure of NUP107 (Figure S11). However, because this protein interacts with many other proteins,[44] the possibility that the p.Asp157Tyr substitution might impair these interactions cannot be excluded, although no such changed

Table 2. *NUP107* Mutations in Affected Individuals with Early-Onset SRNS

Mutation	Amino Acid Change	PolyPhen-2	PyloP	MutationTaster	Grantham	EVS	ExAC	HGVD	In-House Exomes[a] (n = 575)
c.469G>T	p.Asp157Tyr	0.712	2.84	0.998403	160	0	0	0	0
c.969+1G>A	splice site	NA	NA	NA	NA	0	0	0	0
c.1079_1083delAAGAG	p.Glu360Glyfs*6	NA	NA	NA	NA	0	0.0000083	0	0.0008696
c.2492A>C	p.Asp831Ala	1.000	1.952	0.99995	126	0	0	0.0013587	0

Mutations were annotated according to *NUP107* cDNA (GenBank: NM_020401.2). Abbreviations are as follows: EVS, NHLBI Exome Sequencing Project Exome Variant Server; HGVD, Human Genetics Variation Database (the public exome database of the Japanese population).
[a]In-house exome database of Japanese control individuals.

interaction for this particular variant site has been reported. Because the Asp831 side chain forms hydrogen bonds with the Arg842 side chain, the p.Asp831Ala substitution is considered to disrupt these hydrogen bonds. To evaluate the effects of this variant on the structure of NUP107, we performed MD simulations for wild-type and altered NUP107 in solution. In this substitution, a region around the variant site and a region involved in interactions with NUP133 (amino acid residues 881–890) both showed more fluctuations than did those same regions in the wild-type protein (Figure S12). This NUP133-interacting region is considered to be structurally correlated with the variant site through van der Waals contacts (Figure S12B). The results from the MD simulations suggest that the p.Asp831Ala substitution impairs the molecular interaction between NUP107 and NUP133.

Impaired Function of the Altered NUP107

Because NUP107 interacts with NUP133 via its C-terminal tail,[14] we investigated the mutational effects on the protein-protein interaction between NUP107 and NUP133 in vitro. We used an in vitro pull-down assay with recombinant proteins produced in a wheat germ cell-free system to determine the contribution of the C-terminal region of NUP107. Consistent with a previous report,[14] the altered NUP107 that lacked a third of the C-terminal region (amino acids 645–925) did not bind to NUP133 as tightly as wild-type NUP107 under equilibrium conditions (Figure S13). Likewise, two truncated NUP107 proteins with extensively shorter C termini (p.Asp324* and p.Glu360Glyfs*6) also showed weaker binding to NUP133. Notably, a p.Asp831Ala protein with an altered C terminus exhibited significantly reduced binding to NUP133, whereas a p.Asp157Tyr protein with an altered N terminus retained full binding activity (Figure 3A). Wild-type GFP-fused NUP107, which was transiently produced by a mammalian expression vector, was bound to endogenous NUP133 in HeLa cells, and the p.Asp831Ala protein was also bound to NUP133 but weakly in comparison to the wild-type (Figure 3B). Observation of the intracellular localization of altered GFP-NUP107 indicated that the two truncated proteins were distributed mainly in the cytoplasm, whereas the wild-type protein was clearly localized in the nuclear envelope (Figure 3C). The p.Asp831Ala altered protein was localized in the nuclear envelope and cytoplasm (Figure 3C). These results are consistent with the impaired interaction observed between the altered NUP107 and NUP133.

Zebrafish with *nup107* Knockdown Have Glomerular Abnormalities Mimicking SRNS

Reportedly, zebrafish with homozygous *nup107* mutations and morphants with *nup107* knockdown produced with anti-sense MOs each similarly showed a thin pharyngeal skeleton, unfolded intestine, and loss of swim bladder and died on days 5 and 6.[20] However, the specific renal phenotype was not investigated. Therefore, we injected the *nup107*-TB MO or *nup107*-SB MO to create an in-frame (15-bp) deletion at exon 24 to mimic the commonly shared missense mutation (c.2492A>C [p.Asp831Ala]) and then carefully observed the renal phenotype in vivo (Figures S14 and S15). As reported previously,[20] neither of the zebrafish morphants developed edema until they died at around days 5 and 6 (Figure S14A). Furthermore, we sought to identify the glomerular filtration impairment in knockdown zebrafish (*nup107*-TB MO) but did not observe any traces of recognizable protein leakage in glomeruli at 96 hpf (data not shown). Although zebrafish might not be the best animal model for generating renal phenotypes, in a microscopic section of the *nup107*-SB morphant, we were able to find supportive findings in that the glomeruli were generally underdeveloped and showed hypoplastic or poorly organized capillary vessels and mesangial regions (Figures S14C–S14E). Electron microscopy revealed abnormally shaped foot processes and collapse of the capillary lumen in both morphants (Figures S14F–S14K and S16). Because these observations are similar to those from humans with FSGS, the zebrafish morphants might reflect the renal changes caused by the *NUP107* mutation.

Unchanged NPC Localization in Lymphoblastoid Cells from Affected Individuals with *NUP107* Mutations

Reportedly, NUP107 depletion results in decreased or absent NPCs.[29,36] However, a lymphoblastoid cell line derived from affected individuals showed no apparent NPC loss or abnormality by immunohistochemistry analysis (data not shown), which indicates that some residual

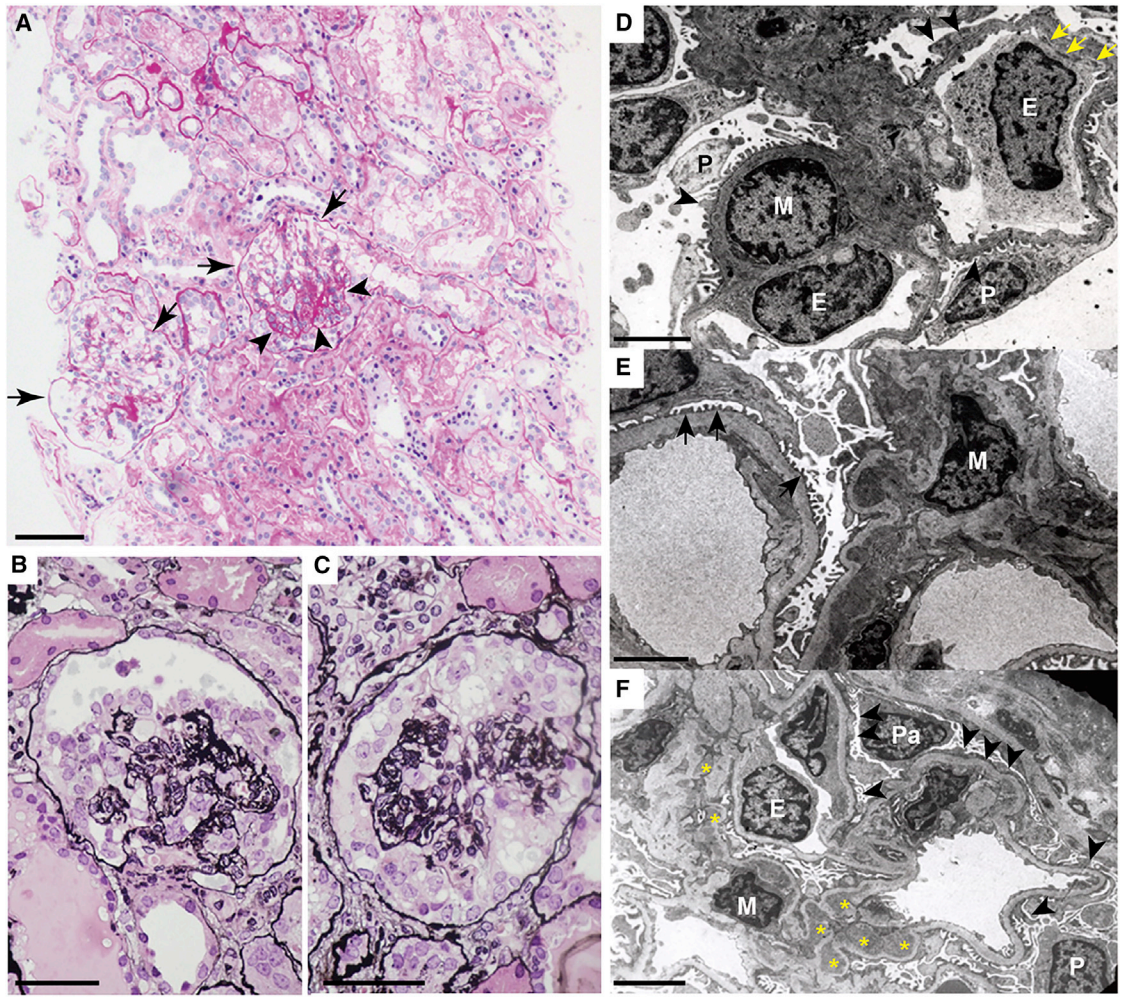

Figure 2. Kidney Histopathology of Affected Individuals with Biallelic *NUP107* Mutations

(A–C) Light micrographs of kidney biopsy specimens from SRNS-TWH II-1. (A) A low-power view (periodic acid-Schiff stain, 100× magnification) of two representative abnormal glomeruli (arrows). Half of the glomerulus is sclerosed (arrowheads). (B and C) Enlarged images (periodic acid methenamine silver stain, 400× magnification) show the collapse of glomerular tufts with hypertrophy and hyperplasia of the glomerular epithelial cells that fill the urinary space. Tubular injury accompanying atrophy of epithelia and interstitial fibrosis is noted.

(D–F) Electron micrographs of biopsy specimens from SRNS-2 II-1 (D), SRNS-2 II-3 (E), and SRNS-2 II-4 (F). Effacement of podocyte foot processes and some mesangial expansion with sub-endothelial electron-dense deposits are apparent. The thickness of the glomerular basement membrane appears normal and shows no evidence of splitting, lamellation, or fragmentation, thereby excluding the possibility of a primary basement-membrane defect. Accumulation of storage materials and dysmorphic mitochondria were not found in the podocyte cytoplasm. Abbreviations are as follows: E, endothelial cell; M, mesangial cell; P, podocyte; Pa, papillary epithelia. Arrowheads indicate effacement of podocyte foot processes, yellow arrows represent electron dense deposits, black arrows show flattened podocyte foot processes, and yellow asterisks show paramesangial deposits.

Scale bars represent100 μm (A), 40 μm (B and C), 2 μm (D and E), and 5 μm (F).

functions of altered NUP107 might persist in the cells of affected individuals, at least under non-stressful conditions. NUP107 is an essential scaffold protein in the NPC, a structure that is evolutionary conserved from yeast to vertebrates.[29,36] Therefore, in the null state, *NUP107* mutants might be lethal in humans.

Discussion

In this study, we have shown that biallelic *NUP107* mutations cause early-onset SRNS in humans. Affected individuals with *NUP107* mutations usually developed SRNS at 2–3 years of age and progressed to ESRD before 10 years of age but experienced no recurrence of the disease after renal transplantation. How do *NUP107* mutations cause a glomerular phenotype in humans? This might be partly explained by the specific properties of podocytes, which are highly differentiated with a unique architecture (foot processes and slit membranes).[45,46] In affected individuals with *NUP107* mutations, insufficient NUP107 function could cause immature and/or hypoplastic podocytes, or at least functionally impaired podocytes that are progressively destroyed by

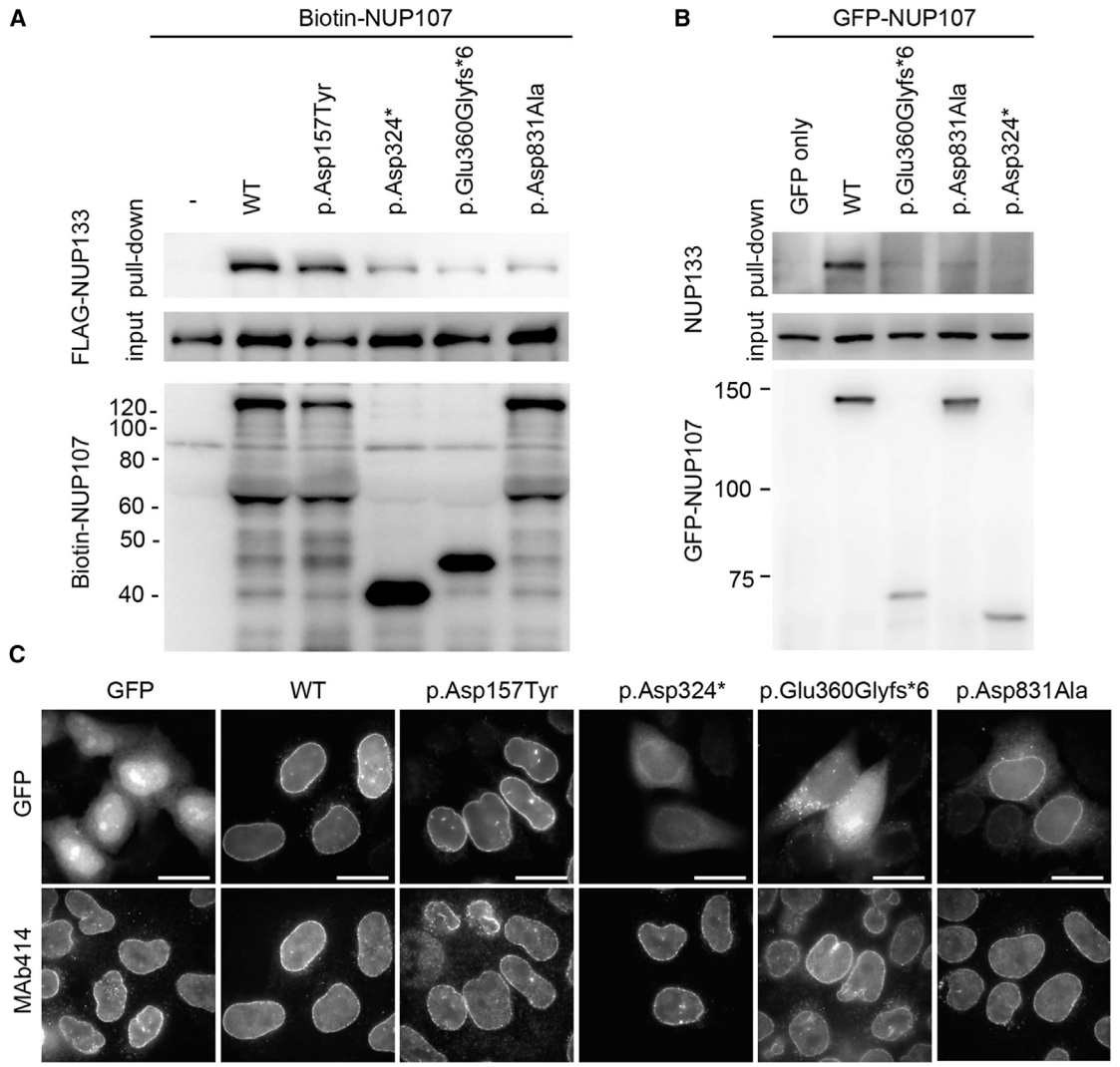

Figure 3. Decreased Intermolecular Interactions between NUP107 and NUP133
(A) In vitro protein-protein binding assay of altered NUP107 with NUP133. The FLAG-tagged NUP133 mixed with biotinylated altered NUP107 proteins was subjected to a pull-down assay with streptavidin magnetic beads. The bound proteins were separated by SDS-PAGE and then detected with an anti-FLAG antibody or with streptavidin-horseradish peroxidase. The corresponding protein inputs are shown in the middle and bottom panels.
(B) Evaluation of the interaction between NUP107 and NUP133 with the use of wild-type NUP107 and its alterations. Wild-type GFP-NUP107 or its alterations were transiently produced in HeLa cells and precipitated with an anti-GFP antibody. The NUP107-NUP133 interaction was analyzed via immunoblotting using the antibodies indicated.
(C) Subcellular localization of NUP107 or its alterations. For visualizing localization of altered or wild-type GFP-NUP107 in HeLa cells, the cells were fixed and stained with a MAb414 antibody recognizing the NPC on the nuclear envelopes. Scale bars represent 20 μm.
The following abbreviation is used: WT, wild-type.

increased filtration pressure after birth. Interestingly, nuclear-envelope proteins, including NPCs, are closely associated with mechanotransduction signaling,[47,48] and mechanical stretching decreases podocyte proliferation and cell-body size by reorganizing the actin cytoskeleton in vitro.[49,50] Thus, increased post-natal capillary pressure leading to mechanical stretching of vulnerable podocytes might accelerate glomerulus damage. Furthermore, mature podocytes do not regenerate.[51,52] Thus, the core pathological condition of SRNS caused by *NUP107* mutations is a structural abnormality, which correlates well with the early SRNS onset in childhood, its steroid resistance, and its lack of post-transplant relapse (Figure S17).

Recently, a homozygous missense mutation (c.303G>A [p.Met101Ile]) was reported in an affected individual who is from a consanguineous family and presents with global developmental delay and early-onset FSGS.[53] However, none of our affected individuals with *NUP107* recessive mutations show neurological impairment. Additional genetic factors might be involved in the neurological symptoms of the consanguineous family. Alternatively, different mutations could cause an additional neurological phenotype. This mutation has been suggested to lead to

abnormal splicing (and possibly a nearly null function), although no direct evidence has been shown.[53] As for p.Asp157Tyr, we could not find direct evidence of its functional impairment experimentally. However, it could be a hypomorphic variant; if so, this might explain the milder phenotype in the SRNS-12 family, who carries both missense mutations (c.469G>T [p.Asp157Tyr] and c.2492A>C [p.Asp831Ala]). Thus, it is possible that the residual NUP107 function left by missense mutations (including c.469G>T [p.Asp157Tyr]) is related to the late onset age and/or milder severity of the disease. It is intriguing that mutations in *NUP107*, which encodes an essential nucleoporin of the NPC, lead to a kidney-specific disease in humans.

In summary, biallelic *NUP107* mutations cause early-onset SRNS for which renal transplantation is the only effective treatment. Access to genetic information is useful for proper clinical management of NS. Therefore, screening *NUP107* mutations in SRNS individuals with broad ranges of clinical severity is strongly encouraged. Furthermore, we did not identify the genetic cause in six pairs of affected siblings and seven single affected individuals in our cohort, which implies a heterogenetic etiology for early-onset SRNS. Further research is necessary to uncover the whole picture of this type of SRNS.

Supplemental Data

Supplemental Data include a supplemental note, 17 figures, and 8 tables and can be found with this article online at http://dx.doi.org/10.1016/j.ajhg.2015.08.013.

Acknowledgments

We are grateful to all the affected individuals and their families who participated in this study. We also thank our clinical colleagues who supported the participating families: Dr. Makoto Endo (Laboratory of Fish Health Management, Tokyo University of Marine Science and Technology) for morphological evaluation of zebrafish and Ms. Sugimoto, Ms. Takabe, and Mr. Mitsui for technical assistance. This work was supported in part by a grant for Research on Measures for Intractable Diseases, a grant for Comprehensive Research on Disability Health and Welfare, and the Strategic Research Program for Brain Science from the Japan Agency for Medical Research and Development; a Grant-in-Aid for Scientific Research on Innovative Areas (Transcription Cycle) (24118007) from the Ministry of Education, Culture, Sports, Science, and Technology of Japan; Grants-in-Aid for Scientific Research (A, B, and C) and for Challenging Exploratory Research from the Japan Society for the Promotion of Science; the fund for Creation of Innovation Centers for Advanced Interdisciplinary Research Areas Program of the Project for Developing Innovation Systems from the Japan Science and Technology Agency; the Takeda Science Foundation; the Osaka Kidney Foundation; and grant HI12C0014 from the Korean Health Technology R&D Project, Ministry of Health & Welfare. K.I. also received grants from Pfizer Japan, Daiichi Sankyo, the Japan Blood Product Organization, Miyarisan Pharmaceutical, AbbVie, CSL Behring, JCR Pharmaceuticals, and Teijin Pharma; and consulting fees from Chugai Pharmaceutical and Astellas Pharma. N.Y. received grants from Novartis Pharma KK and Asahi Kasei Pharma.

Received: June 6, 2015
Accepted: August 28, 2015
Published: September 24, 2015

Web Resources

The URLs for data presented herein are as follows:

1000 Genomes FTP site, ftp://ftp.1000genomes.ebi.ac.uk/vol1/ftp/technical/reference/README.human_g1k_v37.fasta.txt
ExAC Browser, http://exac.broadinstitute.org/
Genome Analysis Toolkit, http://www.broadinstitute.org/gatk
HGVD, http://www.genome.med.kyoto-u.ac.jp/SnpDB/
NHLBI Exome Sequencing Project Exome Variant Server, http://evs.gs.washington.edu/EVS/
Novoalign, http://www.novocraft.com
OMIM, http://www.omim.org
PDB, http://www.rcsb.org/pdb/home/home.do
Picard, http://picard.sourceforge.net
RefSeq, http://www.ncbi.nlm.nih.gov/refseq/
UCSC Genome Browser, https://genome.ucsc.edu/

References

1. Gipson, D.S., Massengill, S.F., Yao, L., Nagaraj, S., Smoyer, W.E., Mahan, J.D., Wigfall, D., Miles, P., Powell, L., Lin, J.J., et al. (2009). Management of childhood onset nephrotic syndrome. Pediatrics *124*, 747–757.
2. Bullich, G., Trujillano, D., Santín, S., Ossowski, S., Mendizábal, S., Fraga, G., Madrid, Á., Ariceta, G., Ballarín, J., Torra, R., et al. (2015). Targeted next-generation sequencing in steroid-resistant nephrotic syndrome: mutations in multiple glomerular genes may influence disease severity. Eur. J. Hum. Genet. *23*, 1192–1199.
3. McKinney, P.A., Feltbower, R.G., Brocklebank, J.T., and Fitzpatrick, M.M. (2001). Time trends and ethnic patterns of childhood nephrotic syndrome in Yorkshire, UK. Pediatr. Nephrol. *16*, 1040–1044.
4. Kim, J.S., Bellew, C.A., Silverstein, D.M., Aviles, D.H., Boineau, F.G., and Vehaskari, V.M. (2005). High incidence of initial and late steroid resistance in childhood nephrotic syndrome. Kidney Int. *68*, 1275–1281.
5. Saleem, M.A. (2013). New developments in steroid-resistant nephrotic syndrome. Pediatr. Nephrol. *28*, 699–709.
6. Zagury, A., Oliveira, A.L., Montalvão, J.A., Novaes, R.H., Sá, V.M., Moraes, C.A., and Tavares, Mde.S. (2013). Steroid-resistant idiopathic nephrotic syndrome in children: long-term follow-up and risk factors for end-stage renal disease. J. Bras. Nefrol. *35*, 191–199.
7. Trautmann, A., Bodria, M., Ozaltin, F., Gheisari, A., Melk, A., Azocar, M., Anarat, A., Caliskan, S., Emma, F., Gellermann, J., et al.; PodoNet Consortium (2015). Spectrum of steroid-resistant and congenital nephrotic syndrome in children: the PodoNet registry cohort. Clin. J. Am. Soc. Nephrol. *10*, 592–600.
8. Lovric, S., Fang, H., Vega-Warner, V., Sadowski, C.E., Gee, H.Y., Halbritter, J., Ashraf, S., Saisawat, P., Soliman, N.A., Kari, J.A., et al.; Nephrotic Syndrome Study Group (2014). Rapid detection of monogenic causes of childhood-onset steroid-resistant nephrotic syndrome. Clin. J. Am. Soc. Nephrol. *9*, 1109–1116.

9. Machuca, E., Benoit, G., and Antignac, C. (2009). Genetics of nephrotic syndrome: connecting molecular genetics to podocyte physiology. Hum. Mol. Genet. *18* (R2), R185–R194.
10. Mekahli, D., Liutkus, A., Ranchin, B., Yu, A., Bessenay, L., Girardin, E., Van Damme-Lombaerts, R., Palcoux, J.B., Cachat, F., Lavocat, M.P., et al. (2009). Long-term outcome of idiopathic steroid-resistant nephrotic syndrome: a multicenter study. Pediatr. Nephrol. *24*, 1525–1532.
11. Sadowski, C.E., Lovric, S., Ashraf, S., Pabst, W.L., Gee, H.Y., Kohl, S., Engelmann, S., Vega-Warner, V., Fang, H., Halbritter, J., et al.; SRNS Study Group (2015). A single-gene cause in 29.5% of cases of steroid-resistant nephrotic syndrome. J. Am. Soc. Nephrol. *26*, 1279–1289.
12. Kitamura, A., Tsukaguchi, H., Iijima, K., Araki, J., Hattori, M., Ikeda, M., Honda, M., Nozu, K., Nakazato, H., Yoshikawa, N., et al. (2006). Genetics and clinical features of 15 Asian families with steroid-resistant nephrotic syndrome. Nephrol. Dial. Transplant. *21*, 3133–3138.
13. Tsurusaki, Y., Koshimizu, E., Ohashi, H., Phadke, S., Kou, I., Shiina, M., Suzuki, T., Okamoto, N., Imamura, S., Yamashita, M., et al. (2014). De novo SOX11 mutations cause Coffin-Siris syndrome. Nat. Commun. *5*, 4011.
14. Boehmer, T., Jeudy, S., Berke, I.C., and Schwartz, T.U. (2008). Structural and functional studies of Nup107/Nup133 interaction and its implications for the architecture of the nuclear pore complex. Mol. Cell *30*, 721–731.
15. Takai, K., Sawasaki, T., and Endo, Y. (2010). Practical cell-free protein synthesis system using purified wheat embryos. Nat. Protoc. *5*, 227–238.
16. Sawasaki, T., Morishita, R., Gouda, M.D., and Endo, Y. (2007). Methods for high-throughput materialization of genetic information based on wheat germ cell-free expression system. Methods Mol. Biol. *375*, 95–106.
17. Sawasaki, T., Kamura, N., Matsunaga, S., Saeki, M., Tsuchimochi, M., Morishita, R., and Endo, Y. (2008). Arabidopsis HY5 protein functions as a DNA-binding tag for purification and functional immobilization of proteins on agarose/DNA microplate. FEBS Lett. *582*, 221–228.
18. Hawryluk-Gara, L.A., Shibuya, E.K., and Wozniak, R.W. (2005). Vertebrate Nup53 interacts with the nuclear lamina and is required for the assembly of a Nup93-containing complex. Mol. Biol. Cell *16*, 2382–2394.
19. Clever, M., Funakoshi, T., Mimura, Y., Takagi, M., and Imamoto, N. (2012). The nucleoporin ELYS/Mel28 regulates nuclear envelope subdomain formation in HeLa cells. Nucleus *3*, 187–199.
20. Zheng, X., Yang, S., Han, Y., Zhao, X., Zhao, L., Tian, T., Tong, J., Xu, P., Xiong, C., and Meng, A. (2012). Loss of zygotic NUP107 protein causes missing of pharyngeal skeleton and other tissue defects with impaired nuclear pore function in zebrafish embryos. J. Biol. Chem. *287*, 38254–38264.
21. Van Der Spoel, D., Lindahl, E., Hess, B., Groenhof, G., Mark, A.E., and Berendsen, H.J. (2005). GROMACS: fast, flexible, and free. J. Comput. Chem. *26*, 1701–1718.
22. Kelley, L.A., and Sternberg, M.J. (2009). Protein structure prediction on the Web: a case study using the Phyre server. Nat. Protoc. *4*, 363–371.
23. Guerois, R., Nielsen, J.E., and Serrano, L. (2002). Predicting changes in the stability of proteins and protein complexes: a study of more than 1000 mutations. J. Mol. Biol. *320*, 369–387.
24. Bussi, G., Donadio, D., and Parrinello, M. (2007). Canonical sampling through velocity rescaling. J. Chem. Phys. *126*, 014101.
25. Darden, T., York, D., and Pedersen, L. (1993). Particle mesh Ewald: An N·log(N) method for Ewald sums in large systems. J. Chem. Phys. *98*, 10089–10092. http://dx.doi.org/10.1063/1.464397.
26. Hess, B., Bekker, H., Berendsen, H.J.C., and Fraaije, J.G.E.M. (1998). LINCS: A linear constraint solver for molecular simulations. J. Comput. Chem. *18*, 1463–1472, 10.1002/(SICI)1096-987X(199709)18:12<1463:AID-JCC4>3.0.CO;2-H.
27. Banerjee, H.N., Gibbs, J., Jordan, T., and Blackshear, M. (2010). Depletion of a single nucleoporin, Nup107, induces apoptosis in eukaryotic cells. Mol. Cell. Biochem. *343*, 21–25.
28. Antonin, W., Ellenberg, J., and Dultz, E. (2008). Nuclear pore complex assembly through the cell cycle: regulation and membrane organization. FEBS Lett. *582*, 2004–2016.
29. Boehmer, T., Enninga, J., Dales, S., Blobel, G., and Zhong, H. (2003). Depletion of a single nucleoporin, Nup107, prevents the assembly of a subset of nucleoporins into the nuclear pore complex. Proc. Natl. Acad. Sci. USA *100*, 981–985.
30. Hoelz, A., Debler, E.W., and Blobel, G. (2011). The structure of the nuclear pore complex. Annu. Rev. Biochem. *80*, 613–643.
31. Weis, K. (2003). Regulating access to the genome: nucleocytoplasmic transport throughout the cell cycle. Cell *112*, 441–451.
32. Fried, H., and Kutay, U. (2003). Nucleocytoplasmic transport: taking an inventory. Cell. Mol. Life Sci. *60*, 1659–1688.
33. Strambio-De-Castillia, C., Niepel, M., and Rout, M.P. (2010). The nuclear pore complex: bridging nuclear transport and gene regulation. Nat. Rev. Mol. Cell Biol. *11*, 490–501.
34. Ori, A., Banterle, N., Iskar, M., Andrés-Pons, A., Escher, C., Khanh Bui, H., Sparks, L., Solis-Mezarino, V., Rinner, O., Bork, P., et al. (2013). Cell type-specific nuclear pores: a case in point for context-dependent stoichiometry of molecular machines. Mol. Syst. Biol. *9*, 648.
35. Bui, K.H., von Appen, A., DiGuilio, A.L., Ori, A., Sparks, L., Mackmull, M.T., Bock, T., Hagen, W., Andrés-Pons, A., Glavy, J.S., and Beck, M. (2013). Integrated structural analysis of the human nuclear pore complex scaffold. Cell *155*, 1233–1243.
36. Walther, T.C., Alves, A., Pickersgill, H., Loïodice, I., Hetzer, M., Galy, V., Hülsmann, B.B., Köcher, T., Wilm, M., Allen, T., et al. (2003). The conserved Nup107-160 complex is critical for nuclear pore complex assembly. Cell *113*, 195–206.
37. González-Aguilera, C., and Askjaer, P. (2012). Dissecting the NUP107 complex: multiple components and even more functions. Nucleus *3*, 340–348.
38. Mundlos, S., Pelletier, J., Darveau, A., Bachmann, M., Winterpacht, A., and Zabel, B. (1993). Nuclear localization of the protein encoded by the Wilms' tumor gene WT1 in embryonic and adult tissues. Development *119*, 1329–1341.
39. Saotome, I., Curto, M., and McClatchey, A.I. (2004). Ezrin is essential for epithelial organization and villus morphogenesis in the developing intestine. Dev. Cell *6*, 855–864.
40. Thong, K.M., Xu, Y., Cook, J., Takou, A., Wagner, B., Kawar, B., and Ong, A.C. (2013). Cosegregation of focal segmental glomerulosclerosis in a family with familial partial lipodystrophy due to a mutation in LMNA. Nephron Clin. Pract. *124*, 31–37.
41. Nagy, V., Hsia, K.C., Debler, E.W., Kampmann, M., Davenport, A.M., Blobel, G., and Hoelz, A. (2009). Structure of a trimeric

nucleoporin complex reveals alternate oligomerization states. Proc. Natl. Acad. Sci. USA *106*, 17693–17698.
42. Fontoura, B.M., Blobel, G., and Matunis, M.J. (1999). A conserved biogenesis pathway for nucleoporins: proteolytic processing of a 186-kilodalton precursor generates Nup98 and the novel nucleoporin, Nup96. J. Cell Biol. *144*, 1097–1112.
43. Loïodice, I., Alves, A., Rabut, G., Van Overbeek, M., Ellenberg, J., Sibarita, J.B., and Doye, V. (2004). The entire Nup107-160 complex, including three new members, is targeted as one entity to kinetochores in mitosis. Mol. Biol. Cell *15*, 3333–3344.
44. Alber, F., Dokudovskaya, S., Veenhoff, L.M., Zhang, W., Kipper, J., Devos, D., Suprapto, A., Karni-Schmidt, O., Williams, R., Chait, B.T., et al. (2007). Determining the architectures of macromolecular assemblies. Nature *450*, 683–694.
45. Pavenstädt, H., Kriz, W., and Kretzler, M. (2003). Cell biology of the glomerular podocyte. Physiol. Rev. *83*, 253–307.
46. Quaggin, S.E., and Kreidberg, J.A. (2008). Development of the renal glomerulus: good neighbors and good fences. Development *135*, 609–620.
47. Swift, J., and Discher, D.E. (2014). The nuclear lamina is mechano-responsive to ECM elasticity in mature tissue. J. Cell Sci. *127*, 3005–3015.
48. Fedorchak, G.R., Kaminski, A., and Lammerding, J. (2014). Cellular mechanosensing: getting to the nucleus of it all. Prog. Biophys. Mol. Biol. *115*, 76–92.
49. Endlich, N., Kress, K.R., Reiser, J., Uttenweiler, D., Kriz, W., Mundel, P., and Endlich, K. (2001). Podocytes respond to mechanical stress in vitro. J. Am. Soc. Nephrol. *12*, 413–422.
50. Petermann, A.T., Hiromura, K., Blonski, M., Pippin, J., Monkawa, T., Durvasula, R., Couser, W.G., and Shankland, S.J. (2002). Mechanical stress reduces podocyte proliferation in vitro. Kidney Int. *61*, 40–50.
51. Kriz, W. (1996). Progressive renal failure–inability of podocytes to replicate and the consequences for development of glomerulosclerosis. Nephrol. Dial. Transplant. *11*, 1738–1742.
52. Nagata, M., Nakayama, K., Terada, Y., Hoshi, S., and Watanabe, T. (1998). Cell cycle regulation and differentiation in the human podocyte lineage. Am. J. Pathol. *153*, 1511–1520.
53. Alazami, A.M., Patel, N., Shamseldin, H.E., Anazi, S., Al-Dosari, M.S., Alzahrani, F., Hijazi, H., Alshammari, M., Aldahmesh, M.A., Salih, M.A., et al. (2015). Accelerating novel candidate gene discovery in neurogenetic disorders via whole-exome sequencing of prescreened multiplex consanguineous families. Cell Rep. *10*, 148–161.

The American Journal of Human Genetics

Supplemental Data

Biallelic Mutations in Nuclear Pore Complex Subunit *NUP107* Cause Early-Childhood-Onset Steroid-Resistant Nephrotic Syndrome

Noriko Miyake, Hiroyasu Tsukaguchi, Eriko Koshimizu, Akemi Shono, Satoko Matsunaga, Masaaki Shiina, Yasuhiro Mimura, Shintaro Imamura, Tomonori Hirose, Koji Okudela, Kandai Nozu, Yuko Akioka, Motoshi Hattori, Norishige Yoshikawa, Akiko Kitamura, Hae Il Cheong, Shoji Kagami, Michiaki Yamashita, Atsushi Fujita, Satoko Miyatake, Yoshinori Tsurusaki, Mitsuko Nakashima, Hirotomo Saitsu, Kenichi Ohashi, Naoko Imamoto, Akihide Ryo, Kazuhiro Ogata, Kazumoto Iijima, and Naomichi Matsumoto

Supplemental Note: Case Reports

These unrelated families are all of Asian origin (four Japanese families, SRNS-1, SRNS-2, SRNS-TK1 and SRNS-TWH1; and one Korean family, SRNS-12) based on their clinical records and interviews (Fig. 1A). Previously, three families, SRNS-1, SRNS-2, SRNS-12, had been reported.[1] The affected individuals show only a kidney-specific phenotype with no abnormal manifestations of other organs, including neurological and sensory features.

SRNS-1

In this family, the older sister (II-2) showed proteinuria at 3 years of age and was treated with steroids. A renal biopsy showed focal glomerulosclerosis of a not-otherwise-specific (NOS) subtype. She died from a varicella zoster virus infection at 3 years of age, before reaching ESRD. The youngest brother (II-4) first developed proteinuria at 3 years, similarly to his affected sister. He received steroid therapy combined with immunosuppressants (cyclosporine [CyA] and cyclophosphamide [CPA]). However, his renal function progressively worsened and he became dialysis-dependent at 9 years of age. He received a renal transplant from his father at 11 years of age and no recurrence of SRNS to date. Parents (I-1, I-2) and two siblings (II-1, II-3) have shown no renal symptoms.

SRNS-2

The extended SRNS family was first recognized by early-onset nephrotic syndrome in the older sister (II-1), who was found to have proteinuria at 2 years of age. She was treated with steroids combined with CyA.

However, she was resistant to drug therapy and progressed to ESRD by age 10 years. The histology of her first renal biopsy at 2 years old showed minimal change but her second biopsy at 4 years revealed FSGS (NOS subtype). At age 10, she underwent a renal transplant of a kidney donated from her father. Subsequently, her two younger identical-twin brothers (II-3 and II-4) displayed early onset SRNS, with a clinical course quite similar that of the older sister (II-1). One brother (II-3) first manifested SRNS at age 2 years. He reached ESRD at 7 years, and received a renal transplant from his mother at that age. The other brother (II-4) took a similar clinical course to his affected siblings, developing SRNS at 2 years and progressing to ESRD at 7 years. He received a cadaveric renal transplantation from his paternal grandmother at 9 years. In all three affected individuals, no post-transplant recurrence of SRNS has been observed.

SRNS-TK1

The first child (II-1) developed nephrotic syndrome at age of 2 years. He was resistant to the standard steroid regimen with CyA and progressed to ESRS at age of 4 years. His renal biopsy at 2 years revealed FSGS. His parents (I-1, I-2) and one brother (II-2) were healthy and had no renal abnormalities. He received a renal transplant at age 7 years from his father, and did not show any recurrence of SRNS.

SRNS-TWH1

The elder sister (II-1) first manifested nephrotic syndrome at 3 years of age. Her renal biopsy revealed a collapsing subtype of FSGS. Despite combination therapy with steroids, angiotensin II receptor blocker (ARB), and plasmapheresis, she rapidly progressed to ESRD at age 4 years. She received a transplanted kidney from her father (I-1). Her younger brother (II-2) exhibited early-onset SRNS quite similar to his

affected sister: He developed a nephrotic condition by age 3 years and received combined immunosuppressive therapy (steroid, CyA and ARB). However, he was resistant to the therapy and had developed ESRD by age 5 years. His renal pathology at age 3 years was a collapsing subtype of FSGS. He is currently treated by peritoneal dialysis, waiting for renal transplantation.

SRNS-12

This SRNS family has been previously reported.[1] The third daughter (II-3; proband) first manifested nephrotic syndrome at the age of 11 years. Her renal biopsy revealed NOS subtype of FSGS. Despite combined therapy with steroids and ARB, she rapidly progressed to ESRD by age 12 years and thereafter started peritoneal dialysis. She received a kidney transplant from her father at age 14 years. She has not developed NS in the 10 years since her kidney transplantation.

The second daughter (II-2) developed proteinuria at age 10 years. However, her clinical course was milder than that of her younger sister, the third daughter (II-3) who reached ESRD only 1 year after the onset of SRNS. She has never produced nephrotic proteinuria, nor received immunosuppressive therapy. Her subnephrotic-range proteinuria (1.4–4.0 g per gram creatinine) has persisted over the last 10 years. Renal biopsy has not yet been performed. Her renal function has been preserved compared to her younger sister (II-3), but has gradually declined from eGFR 85.5 ml/min (at age 32 years) to 62.2 ml/min (at her current age of 34 years) under administration of ARB alone (losartan 50 mg/day). The parents (I-1, I-2) and eldest daughter (II-1) have not shown any renal symptoms.

Figure S1

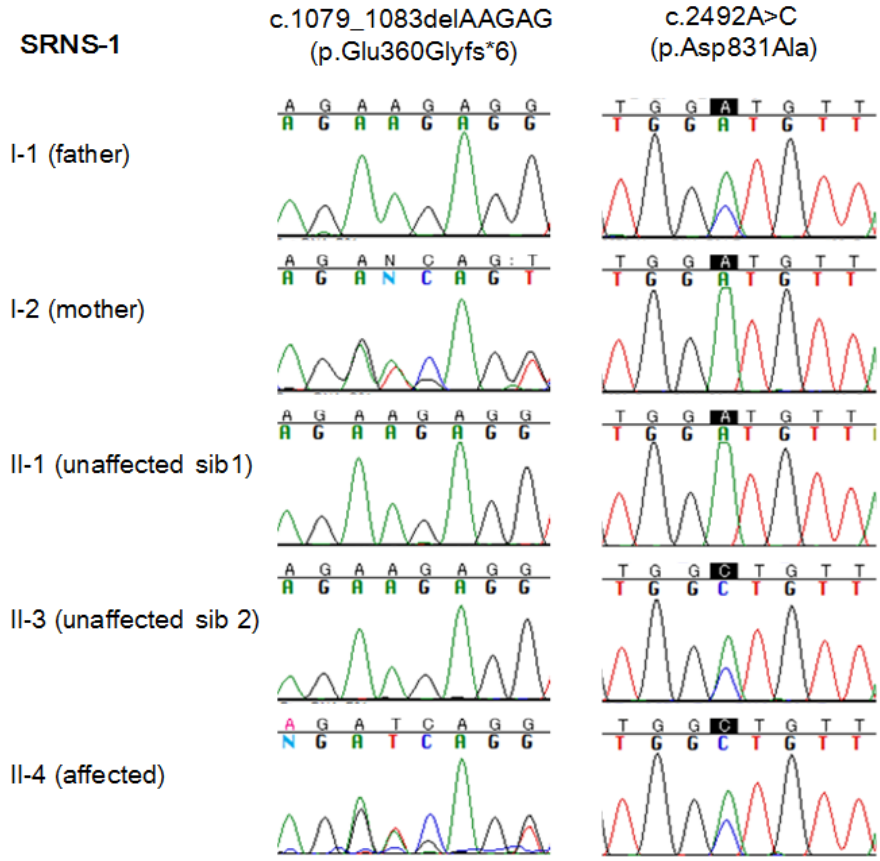
SRNS-1
c.1079_1083delAAGAG
(p.Glu360Glyfs*6)
c.2492A>C
(p.Asp831Ala)
I-1 (father)
I-2 (mother)
II-1 (unaffected sib1)
II-3 (unaffected sib 2)
II-4 (affected)

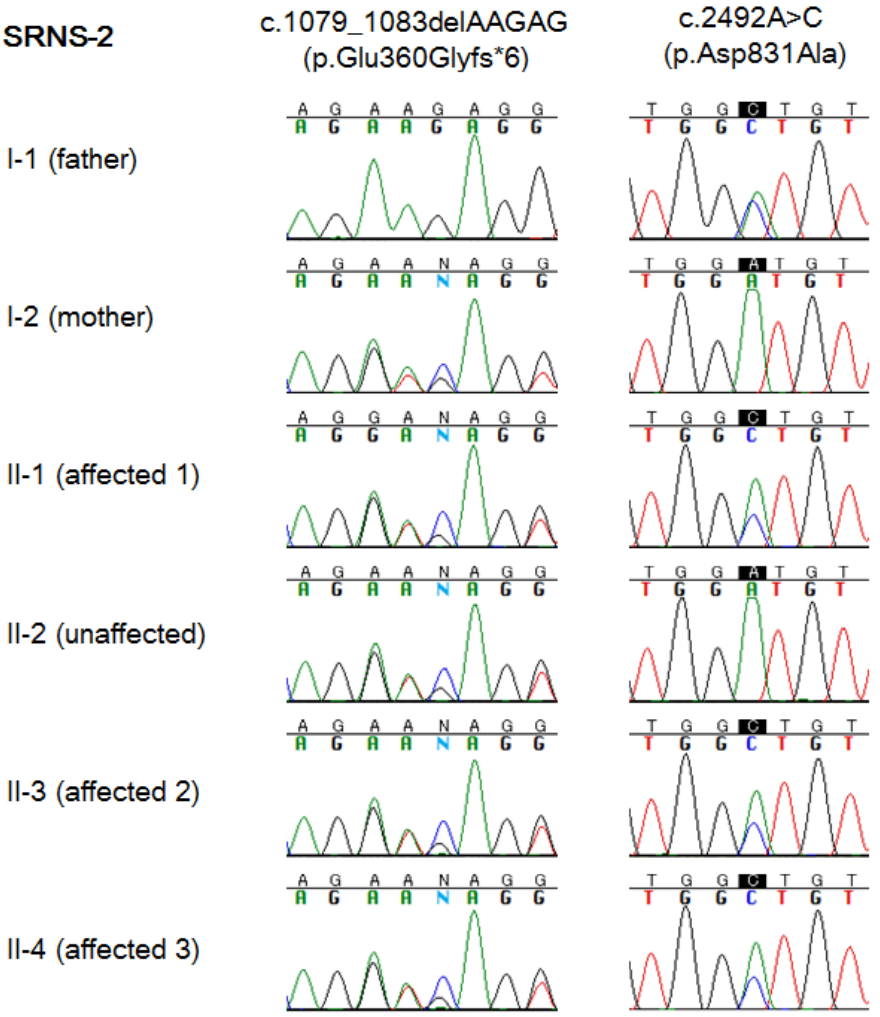
SRNS-2
c.1079_1083delAAGAG
(p.Glu360Glyfs*6)
c.2492A>C
(p.Asp831Ala)
I-1 (father)
I-2 (mother)
II-1 (affected 1)
II-2 (unaffected)
II-3 (affected 2)
II-4 (affected 3)

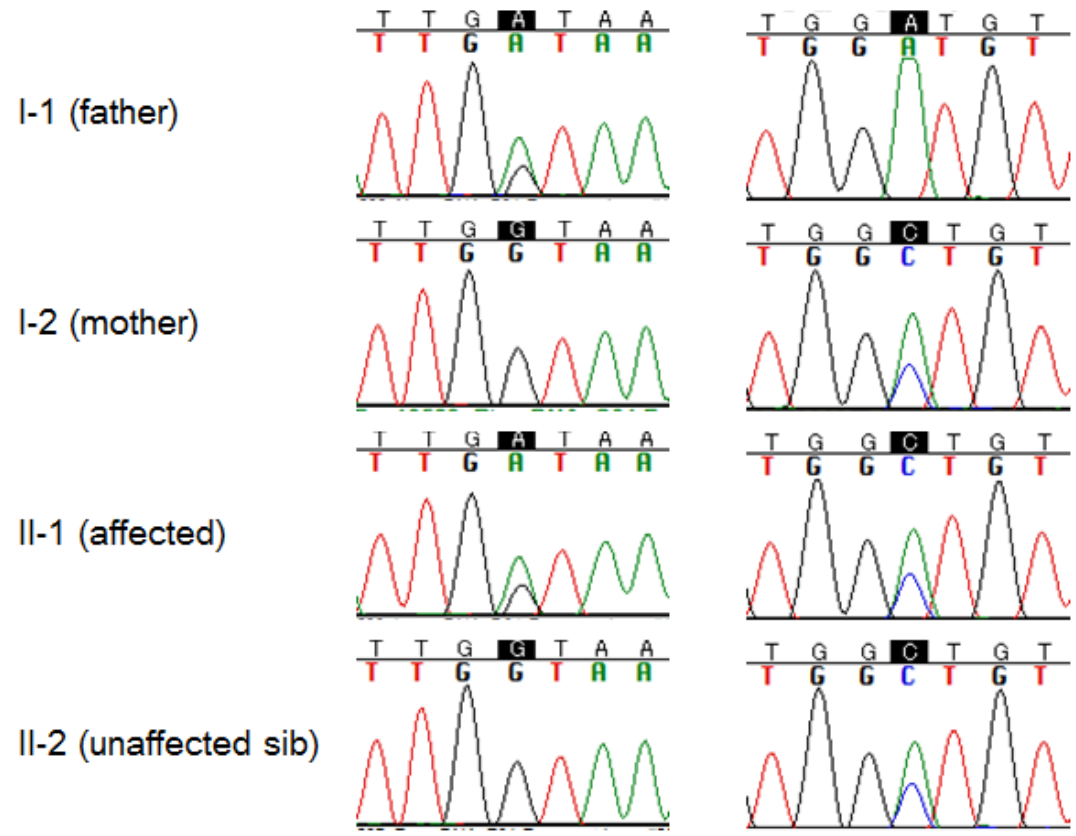
SRNS-TK1
c.969+1G>A
c.2492A>C
(p.Asp831Ala)
I-1 (father)
I-2 (mother)
II-1 (affected)
II-2 (unaffected sib)

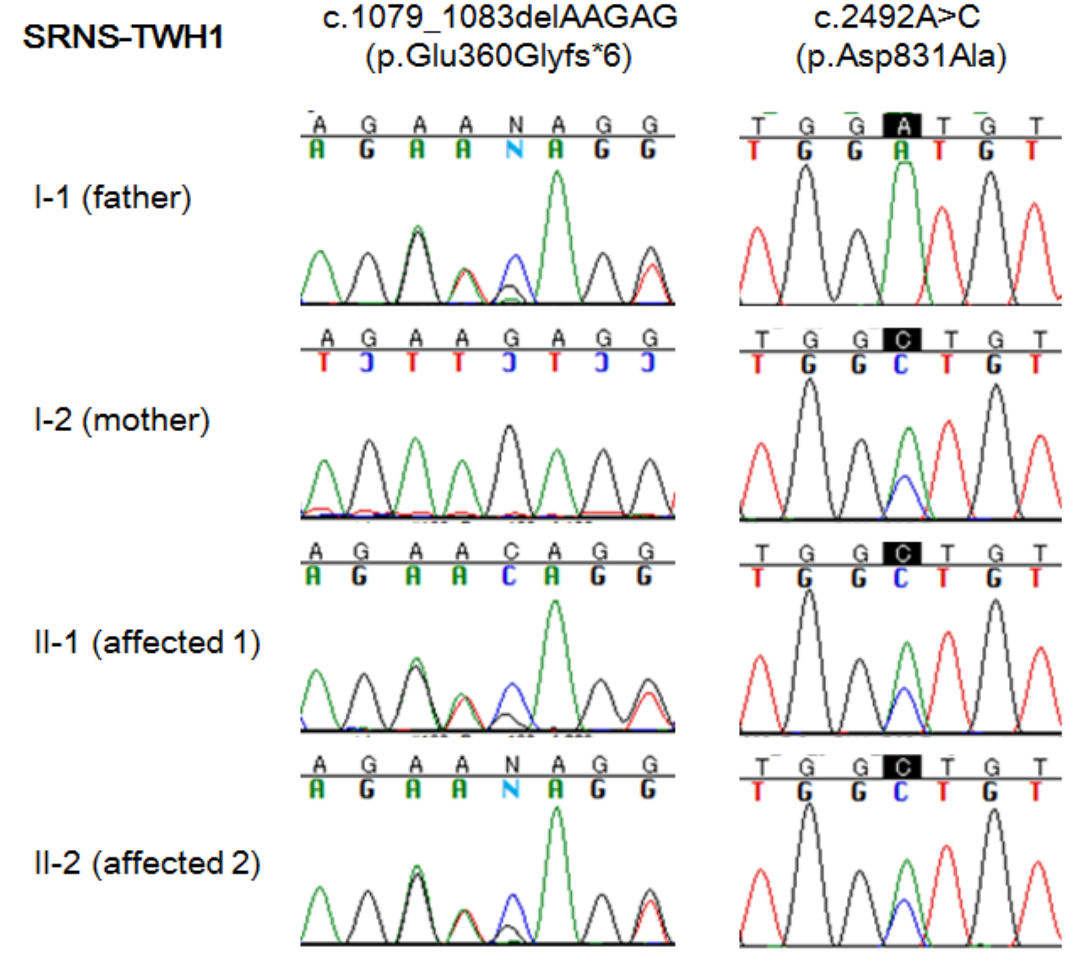
SRNS-TWH1
c.1079_1083delAAGAG
(p.Glu360Glyfs*6)
c.2492A>C
(p.Asp831Ala)
I-1 (father)
I-2 (mother)
II-1 (affected 1)
II-2 (affected 2)

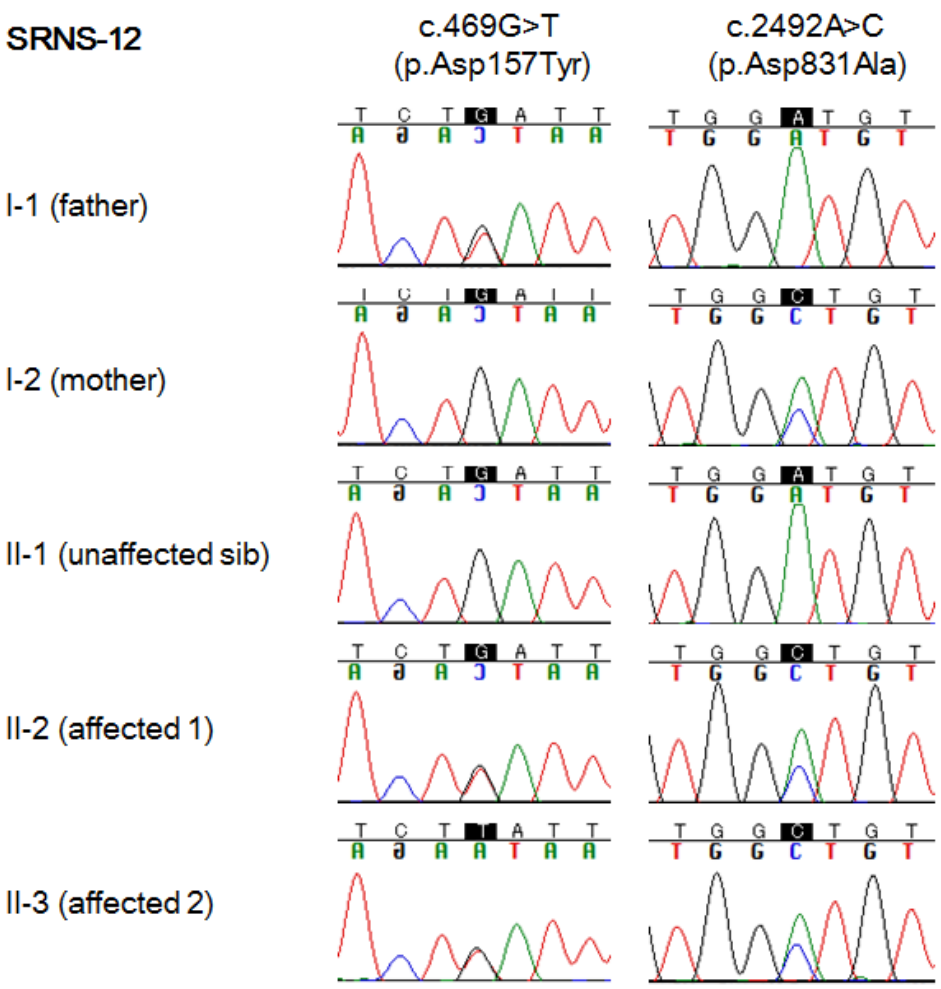

Figure S1. Electropherograms of *NUP107* Mutations Found in Families with Early-Onset Steroid-Resistant Nephrotic Syndrome

Compound heterozygous mutations co-segregated completely with all the affected individuals in the five families.

Figure S2

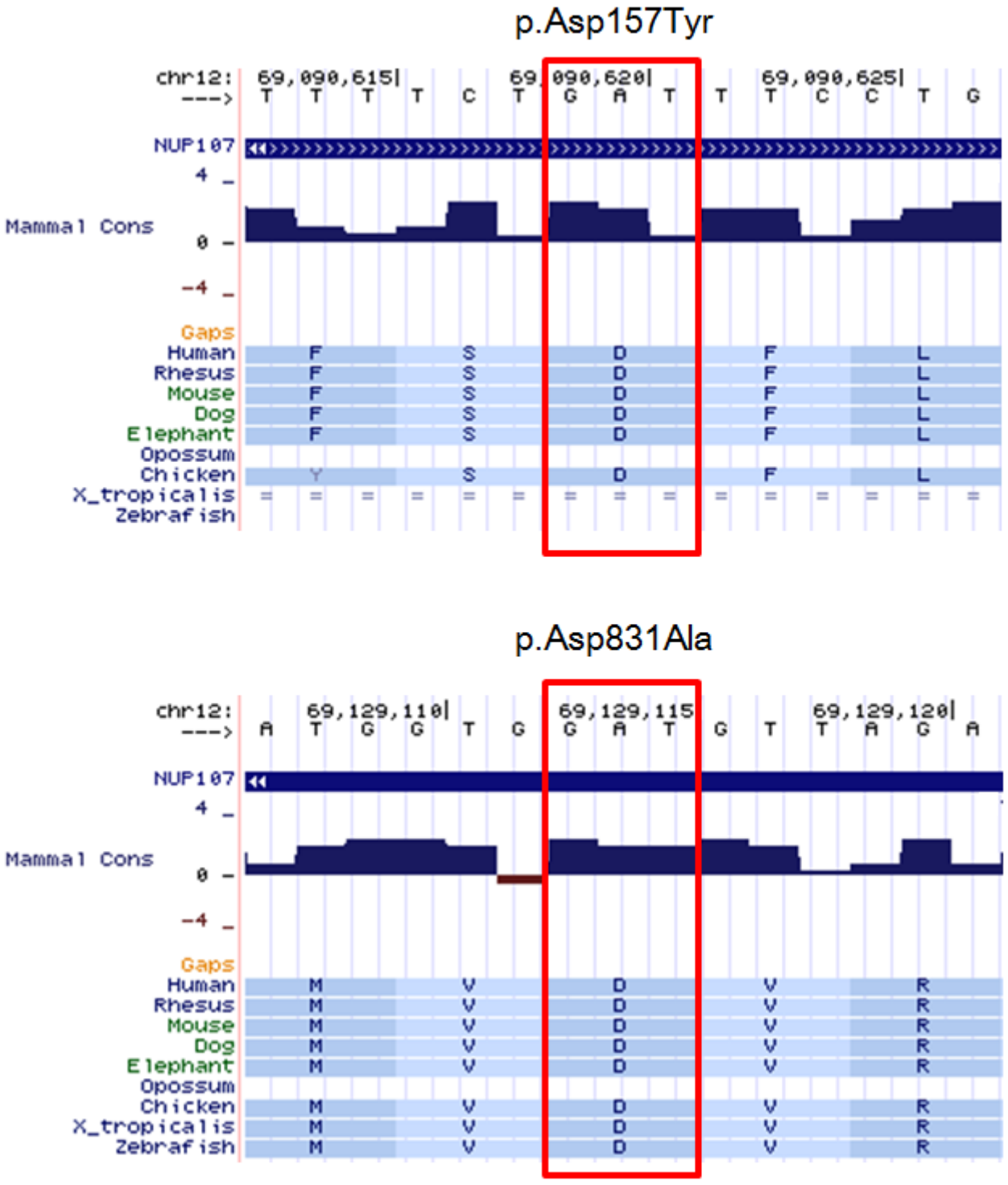

Figure S2. Evolutionary Conservation of the Amino Acids Altered by Two Missense Mutations

The amino acids altered in the affected individuals are evolutionally conserved from chickens to humans (p.Asp157) and from zebrafish to humans (p.Asp831).

Figure S3

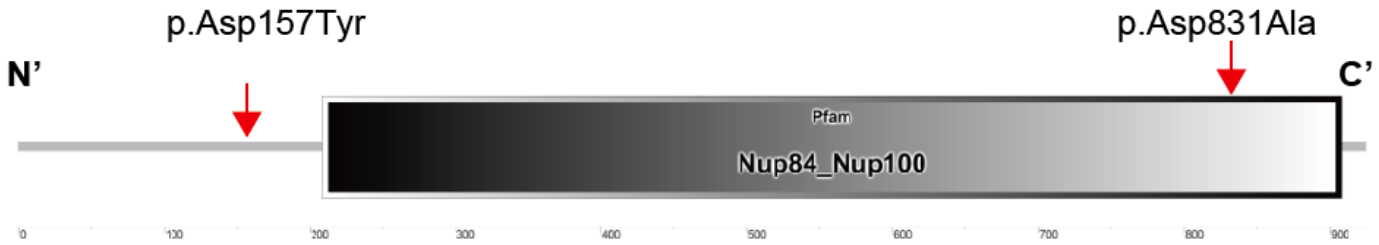

Figure S3. Locations of the Two Missense Mutations in NUP107

The region from 209 to 908 amino acids was defined as the Nup84_Nup100 domain by the SMART program (http://smart.embl-heidelberg.de/) using NUP107 protein sequence (NP_065134). p.Asp831Ala is localized within this domain.

Figure S4

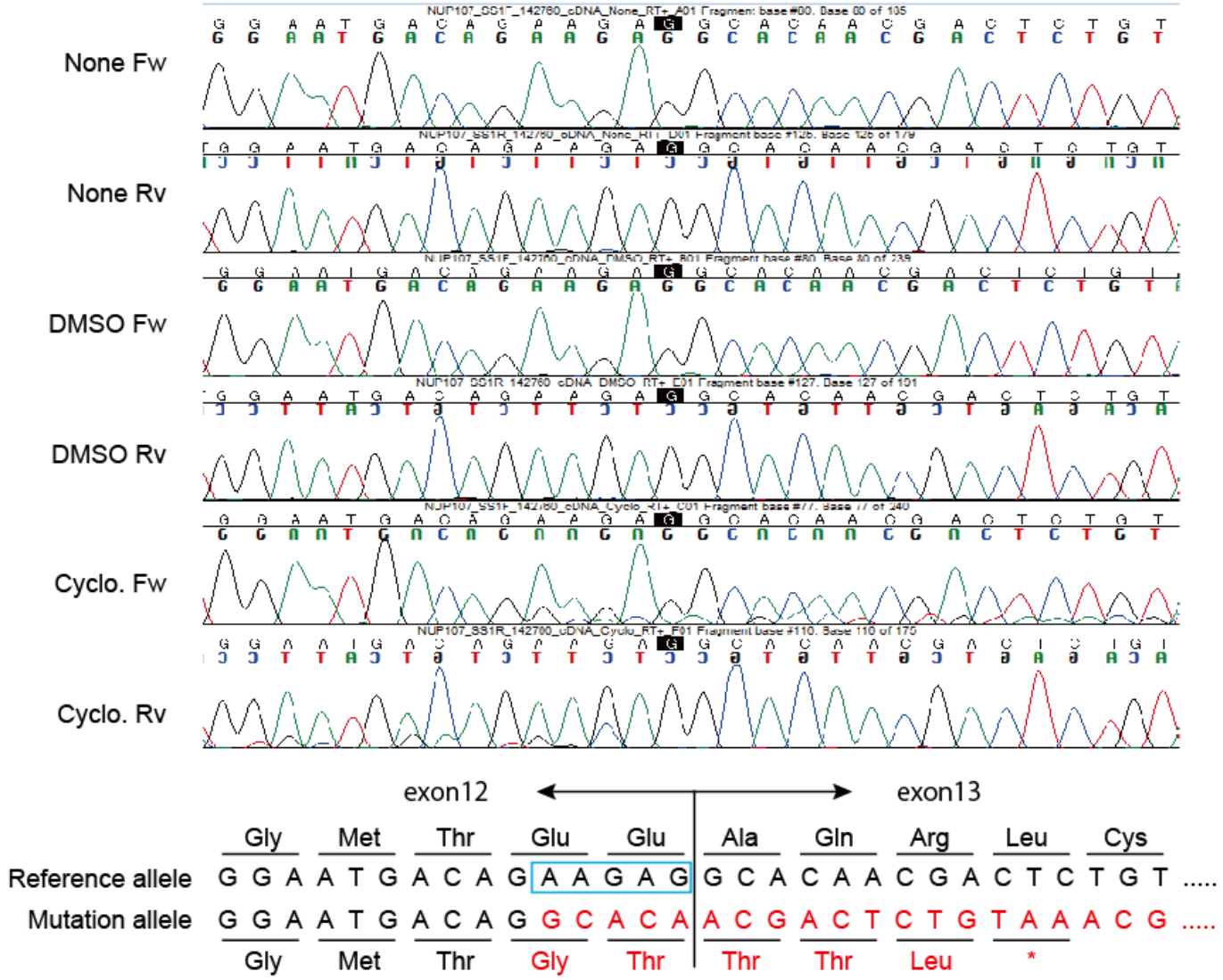

Figure S4. Nonsense Mediated mRNA Decay by the 5-bp Deletion (c.1079_1083delAAGAG)

These chromatograms are from SRNS-TWH II-2. The 5-bp deletion (marked by the blue box) resulted in nonsense-mediated mRNA decay of the mutant allele as the cDNA sequence of the mutant allele can be seen only after treatment with cycloheximide.

Figure S5

[Splice site prediction by Neural Network]

Donor site predictions for WT :

Start	End	Score	Exon	Intron
710	724	0.57	ggctgca	gtgagtca
1202	1216	0.80	tgaattg	gtaaatgt
1302	1316	0.80	tctaaag	gtttgcac
1392	1406	0.91	ttgaatt	gtaagtaa
1485	1499	0.70	atataag	gtagtgac
1558	1572	0.93	gtttgag	gttagaac

Donor site predictions for Mut :

Start	End	Score	Exon	Intron
710	724	0.57	ggctgca	gtgagtca
1302	1316	0.80	tctaaag	gtttgcac
1392	1406	0.91	ttgaatt	gtaagtaa
1485	1499	0.70	atataag	gtagtgac
1558	1572	0.93	gtttgag	gttagaac

[NetGene2 v. 2.4]

WT

```
Donor splice sites, direct strand
---------------------------------
                pos 5'->3'  phase strand  confidence  5'      exon intron    3'
                   1209        0      +        0.42        CACTGAATTG^GTAAATGTTC
                   1399        2      +        0.32        CCTTTGAATT^GTAAGTAATA
                   1565        0      +        0.00        TTGGTTTGAG^GTTAGAACGG
```

Mut

```
Donor splice sites, direct strand
---------------------------------
                pos 5'->3'  phase strand  confidence  5'      exon intron    3'
                   1399        2      +        0.32        CCTTTGAATT^GTAAGTAATA
                   1565        0      +        0.00        TTGGTTTGAG^GTTAGAACGG
```

Figure S5. *In silico* Prediction of the Splicing Abnormality Caused by c.969+1G>A

The upper and lower panels show the splice sites predicted by NNSPLICE 0.9 (http://www.fruitfly.org/seq_tools/splice.html) and NetGene2 v. 2.4 (http://www.cbs.dtu.dk/services/NetGene2/), respectively. The canonical donor site in the wild-type allele marked by red boxes (based on the two prediction programs) is abolished in the mutant allele.

Figure S6

					SRNS-1	SRNS-2	SRNS-TK1	SRNS-TWH1	SRNS-12
#CHROM	POS	ID	REF	ALT	II-4	II-1	II-1	II-1	II-3
12	66838243	rs10878422	A	G	G	G	G	G	G
12	67706466	rs1060350	G	A	G	G	G	G	G
12	68045403	rs10878641	G	A	A	A	G	G	A
12	68052178	rs3741644	G	T	T	(T)	T	T	T
12	68372071	rs7299287	C	A	A	(A)	A	A	(A)
12	68595719	rs10748100	T	C	T	C	T	T	(T)
12	68595787	rs10748101	A	G	A	G	A	A	(A)
12	68646521	rs2227491	T	C	T	C	T	T	(T)
12	68688939	rs7958232	C	T	T	(T)	T	T	(T)
12	68707576	rs4575357	G	A	A	(A)	A	A	G
12	68708761	rs2306393	C	T	T	(T)	T	T	(T)
12	68719216	rs2870812	G	A	A	(A)	A	A	(A)
12	68720627	rs962976	G	A	A	(A)	A	A	(A)
12	68721040	rs962977	A	G	G	(G)	G	G	(G)
12	68724951	rs3741808	G	T	T	(T)	T	T	(T)
12	68867496	.	T	TA	TA	TA	TA	TA	TA
12	68868056	rs9325188	A	G	G	G	G	G	G
12	68868289	rs2015278	G	A	A	A	A	A	A
12	68881347	rs7307851	C	G	G	G	G	G	G
12	68881563	.	TC	T	T	T	T	T	T
12	69129114	c.2492A>C	A	C	C	C	C	C	C
12	69207162	rs1470383	G	A	A	A	A	A	A
12	69208578	rs1846402	A	C	C	C	C	C	C
12	69218038	rs2291857	T	G	G	G	G	G	G
12	69250548	rs3741598	C	T	T	T	T	T	T
12	69261044	rs1144949	C	T	T	T	T	T	T
12	69279736	rs2701085	A	G	G	G	G	G	G
12	69633379	rs2305642	A	G	G	G	G	G	(G)
12	69645864	rs490872	A	G	G	G	G	G	(G)
12	69646010	rs607797	T	C	C	C	C	C	(C)
12	69652336	.	G	GT	GT	GT	GT	GT	(GT)
12	69653146	rs2231700	T	C	C	C	C	C	(C)
12	69667075	rs1463335	T	A	A	A	A	A	(A)
12	69678311	.	T	C	C	C	C	C	C
12	69747177	rs710794	C	T	T	T	T	T	T
12	69753595	rs622656	C	T	C	T	C	T	C
12	69759551	.	AT	A	AT	A	AT	A	AT
12	69967636	rs512853	C	T	T	T	T	T	T
12	69979127	rs17106752	G	A	G	A	G	G	(G)
12	69980028	rs485288	G	A	A	A	A	A	A
12	69980141	rs484319	G	C	C	C	C	C	C
12	69980434	rs80262100	C	T	C	T	C	C	(C)
12	69981862	rs530701	G	A	A	A	A	A	A
12	69987494	rs710773	G	A	A	A	A	A	A
12	69991627	rs710765	C	T	T	T	T	T	T
12	69991675	rs35639	T	C	T	C	T	T	(T)
12	70070942	rs710718	A	G	G	G	G	G	G
12	70078124	rs710715	G	C	C	C	C	G	C
12	70078172	rs710714	C	T	T	T	T	C	T
12	70088085	.	AGT	A	AGT	A	AGT	AGT	AGT
12	70091432	rs775429	T	C	C	C	C	C	C
12	70190408	rs17120917	A	C	C	(C)	A	A	A
12	70273303	rs1240286	C	G	G	G	G	G	G
12	70274160	.	G	A	A	A	A	A	A

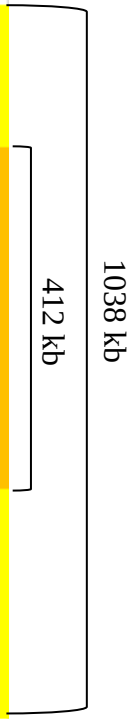

Figure S6. A Common Haplotype That Harbors c.2492A>C (p.Asp831Ala) Was Found in the Five SRNS Families

The confirmed mutation-specific haplotype (412 kb in size) highlighted in orange is common to all the families. The yellow highlighted region together with orange highlighted region (1038 kb in size) could be

considered the common haplotype if the inferred SNPs within parentheses are included, as parental exome data were unavailable for SRNS-2 and SRNS-12.

Figure S7

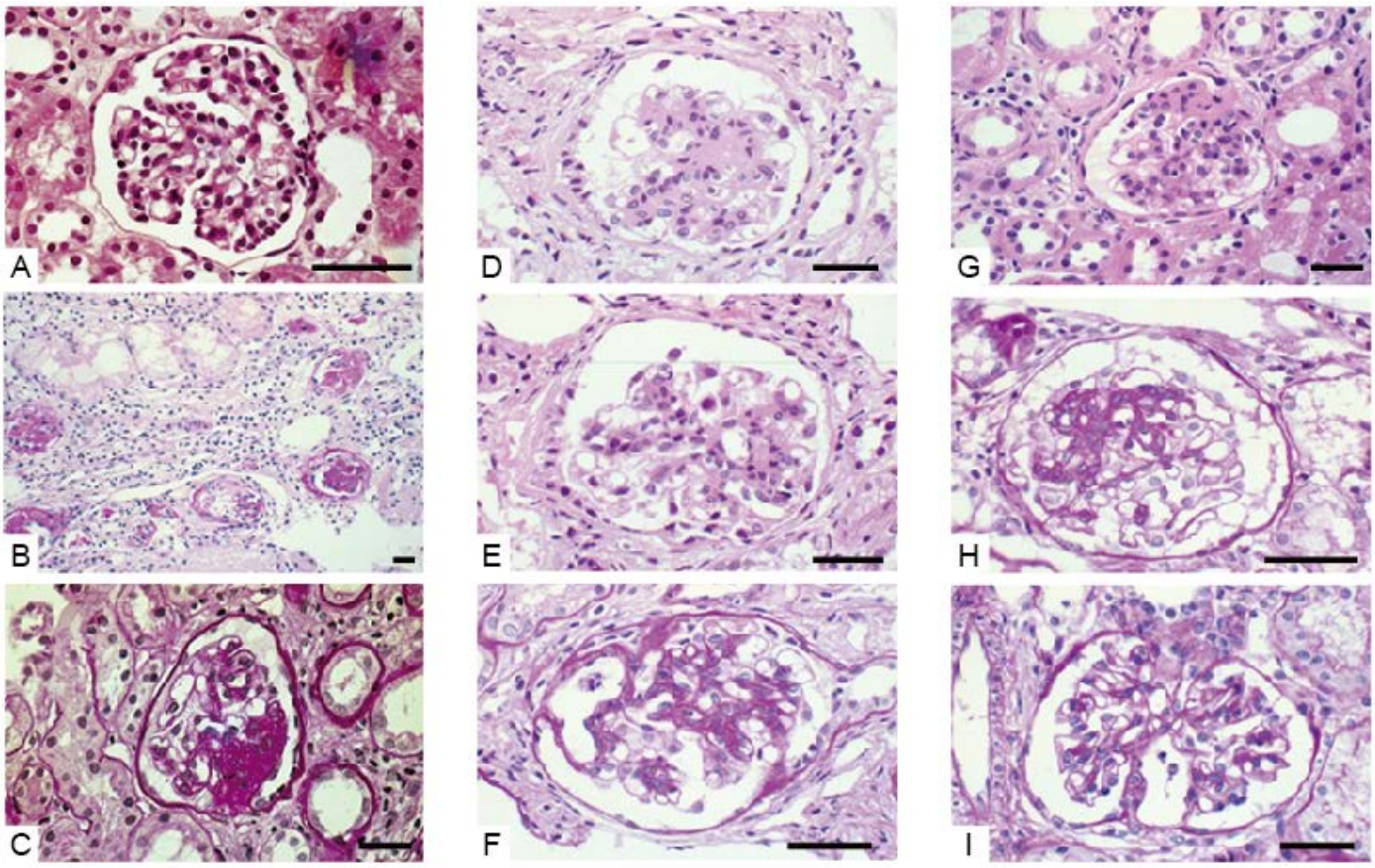

Figure S7. Histopathological Images of Renal Biopsies from Affected Individuals in the SRNS-2 Family

SRNS-2 II-1 underwent renal biopsies at ages 2 years (A) and at 4 years (B, C). The sclerotic changes became more prominent at 4 years of age. Biopsied samples of SRNS-2 II-3 (D, E, F) and SRNS-2 II-4 (G, H, I) stained with periodic Acid Schiff show focal segmental glomerulosclerosis [image magnifications: ×100 (b), ×400 (a, c–i)]. Scale bars: 40 μm.

Figure S8

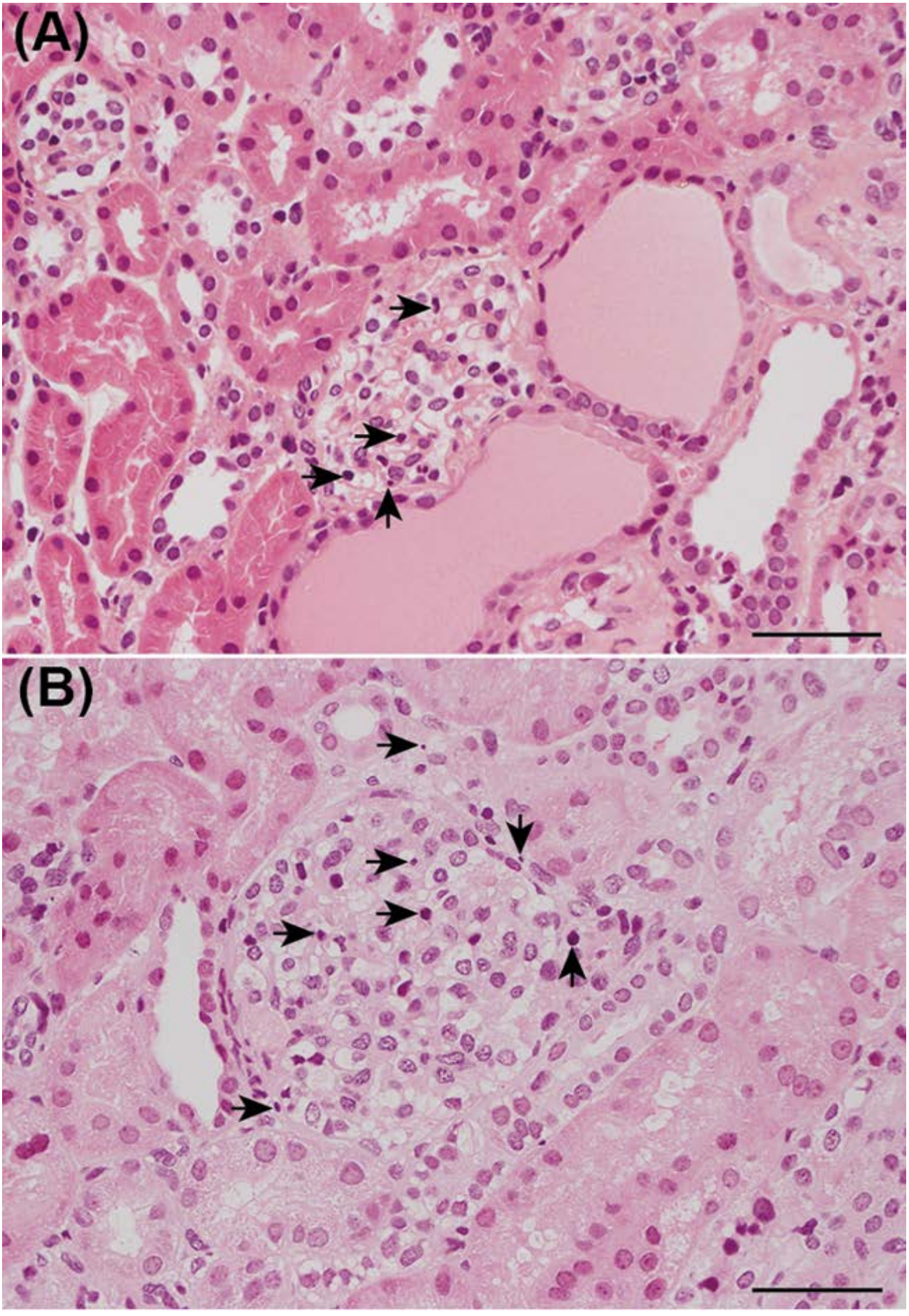

Figure S8. Hematoxylin and Eosin-Stained Kidney Tissues from Affected Individuals in the

SRNS-TWH1 Family

These images are from SRNS-TWH1 II-1 (A) and SRNS-TWH1 II-2 (B). Cells that showed nuclear shrinkage and fragmentation were occasionally found in the glomeruli and renal tubules (arrows). Scale bars: 50 μm.

Figure S9

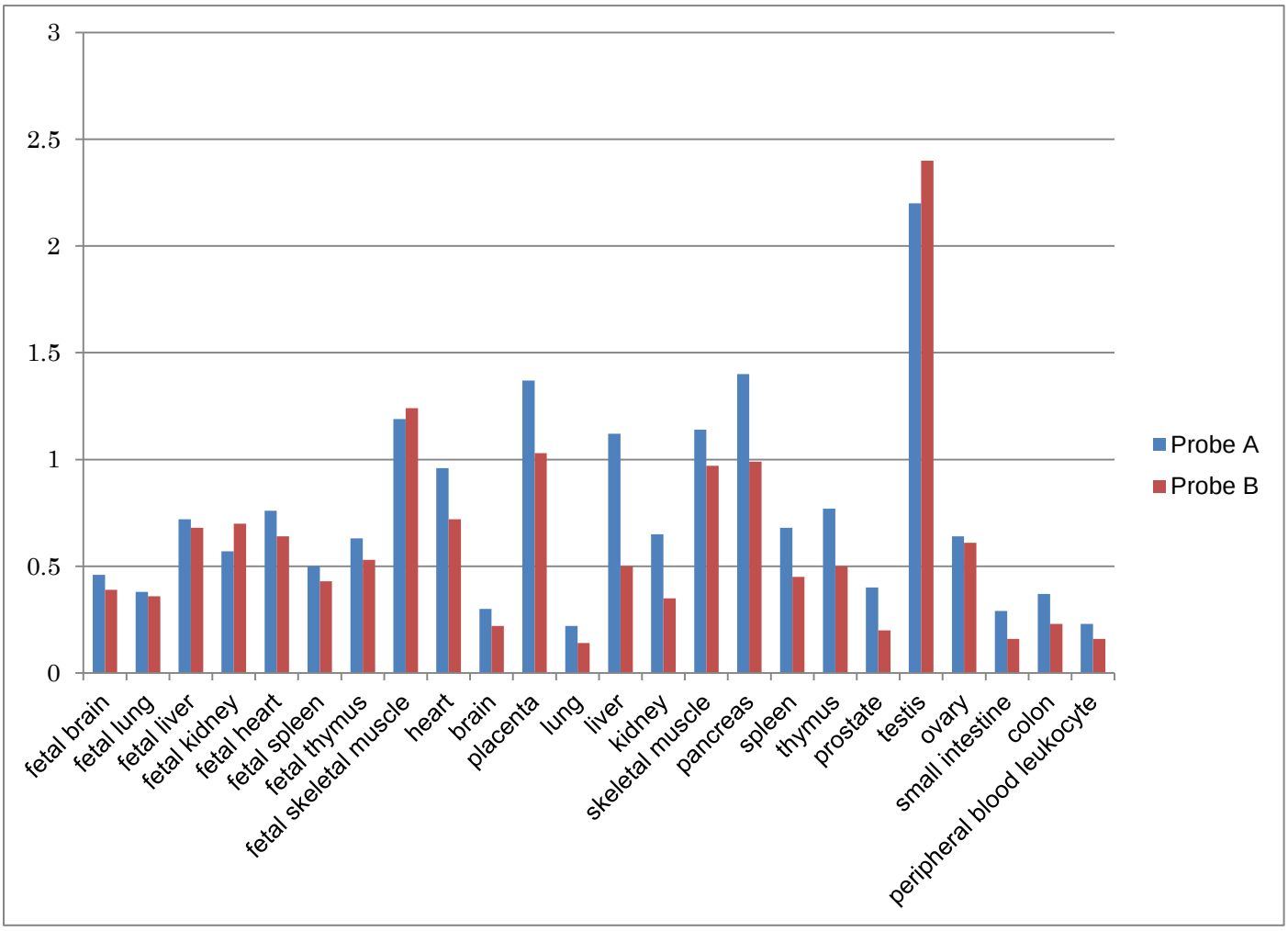

Figure S9. Quantitative *NUP107* Expression Analysis in Fetal and Adult Tissues Using TaqMan Assays

TaqMan Probes A (Hs00914854_g1) and B (Hs00220703_m1) show similar *NUP107* expression levels in various tissues. The Y-axis represents the relative expression levels normalized against beta-actin expression levels.

Figure S10

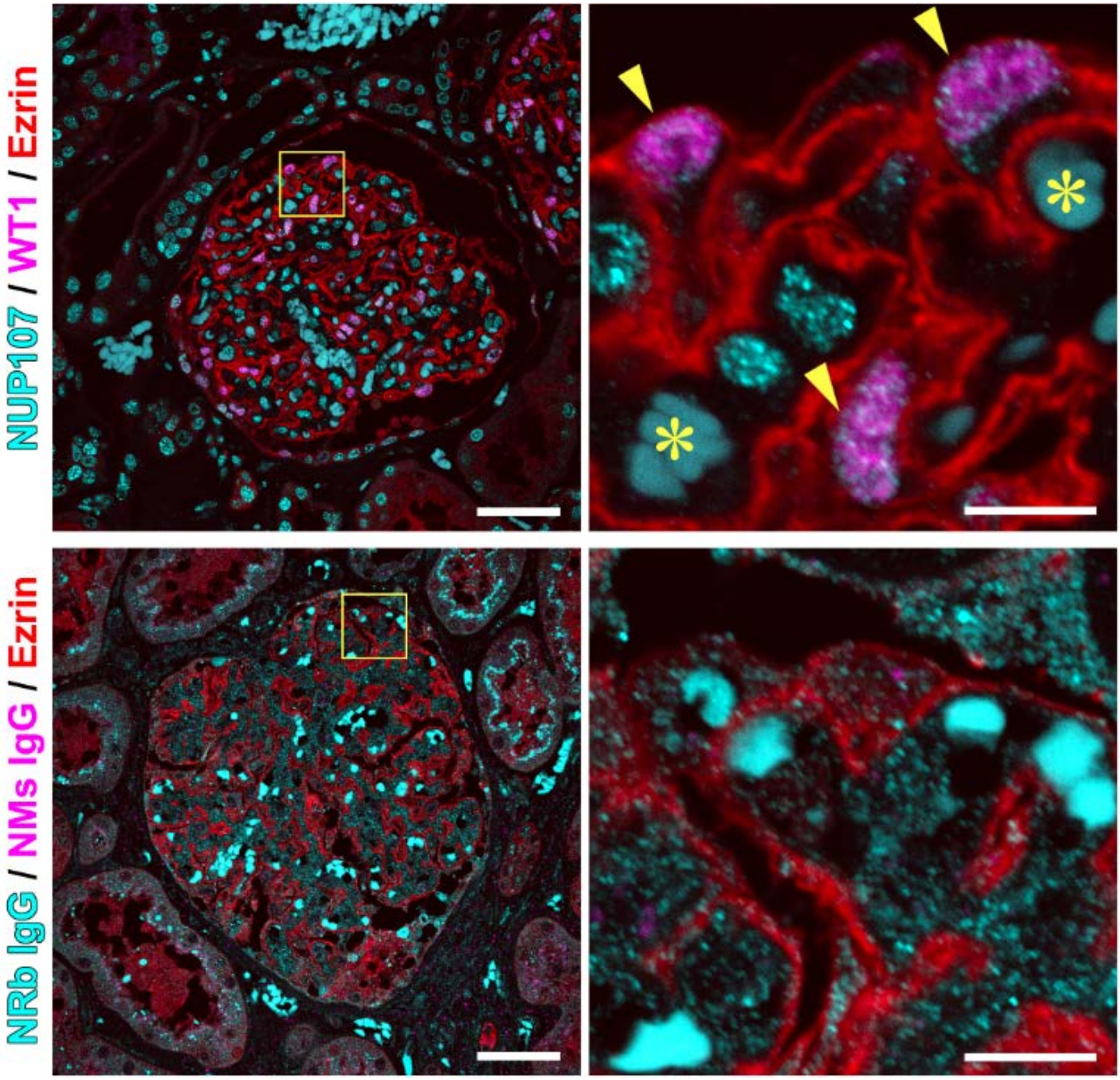

Figure S10. Nuclear localization of NUP107 in podocytes

Podocytes in human kidney sections were identified using antibodies against WT1 (magenta) and Ezrin (red) (upper panels). Boxed regions are enlarged (right) to show the speckle-like nuclear distribution of NUP107 in more detail. A single optical section shows the glomerular capillary tufts to be covered with podocytes; their nuclei on the glomeruli surfaces contain WT1 and NUP107 (arrow heads). Asterisks: autofluorescent

erythrocytes in the capillary lumen. Normal rabbit IgG (NRb IgG) and normal mouse IgG (NMs IgG) were used for negative controls (lower panels). Scale bars: 50 μm (left); 10 μm (right).

Figure S11

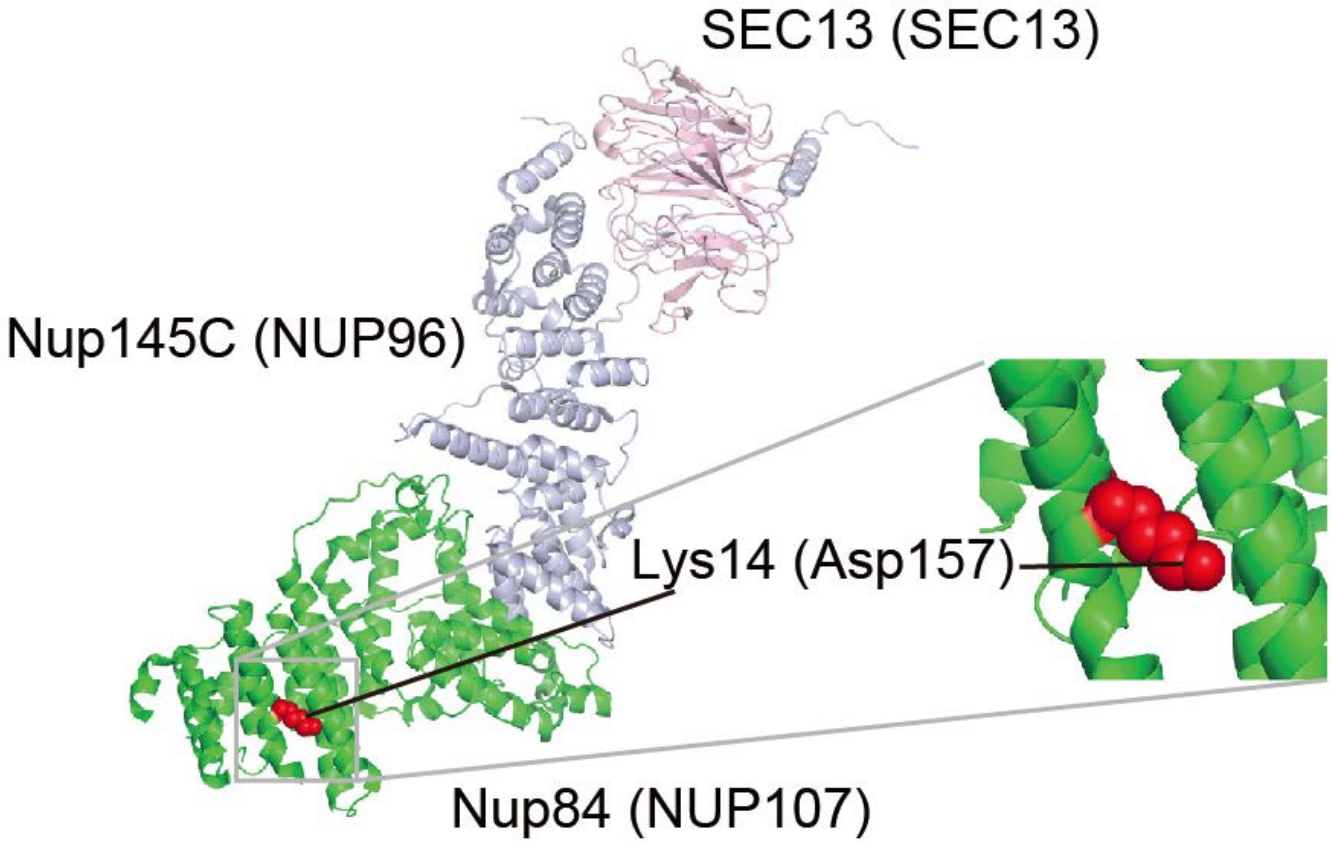

Figure S11. Location of the p.Asp157 Missense Substitution

Crystal structure of yeast Sec13 (amino acid residues 1–297, light pink)-Nup145C (731–1158, light blue)-Nup84 (1–460, green) complex (PDB code; 3IKO) is shown with a magnified view around the variant site in Nup84, which is the yeast homolog of human NUP107. Each component of the complex is annotated with the corresponding human homologs in parentheses. Lys 14 of yeast Nup84 (Asp 157 of human NUP107) is colored red; its side chain is shown as a van der Waals representation.

Figure S12

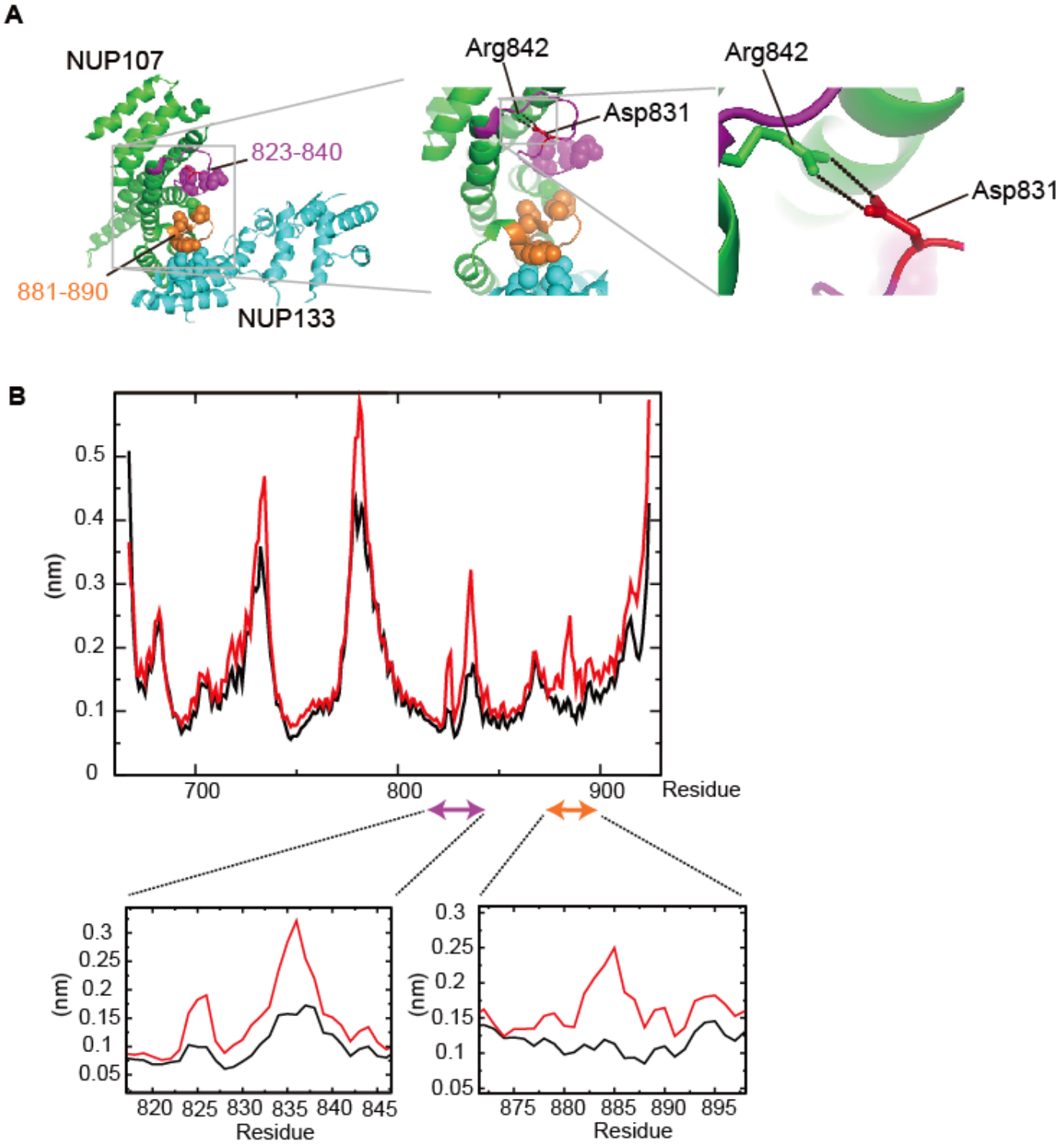

Figure S12. Molecular Structure Effects Caused by Replacement of Residue Asp831 in NUP107

(A) Crystal structure of the nucleoporin NUP107-NUP133 complex (PDB code 3CQC), which includes the human NUP107 fragment (containing an amino acid region at 658–925, in green except for the regions described below), and the human NUP133 fragment (containing the amino acid region 935–1156, in cyan),

which is shown with magnified views of the squared regions. A residue at the mutation site, Asp 831 (in red), and amino acid regions 823–840 (in magenta) and 881–890 (in orange), are predicted by the molecular dynamics simulation to cause a structural perturbation of the p.Asp831Ala mutation (see main text). Side chains of some hydrophobic residues that are involved in these two regions are shown in a van der Waals sphere representation; those of Asp 831 and Arg 842 are depicted as sticks. Black dotted lines represent hydrogen bonds. (B) Root mean squared fluctuation (RMSF) plots of NUP107 along the MD simulations. The RMSFs of the backbone atoms of the wild-type NUP107 fragment (amino acid residues 685–925; in black) and its Asp831Ala variant (red) are plotted. Graphic scales corresponding to amino acid regions 815–847 and 873–897 are magnified.

Figure S13

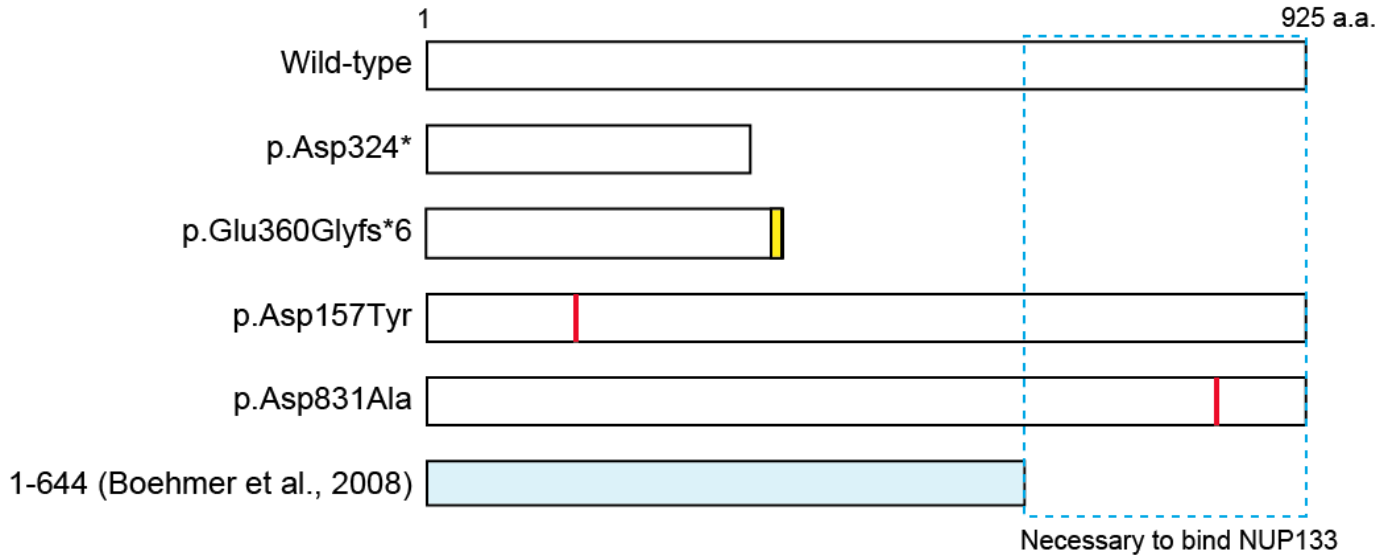

Figure S13. Schematic of the NUP107 Constructs Illustrating the Mutation Positions

Wild-type and four mutant *NUP107* constructs were subcloned into a mammalian expression vector. The shorter protein (light blue box, 1–644 amino acids) cannot bind to NUP133.[2] The blue dotted rectangular region is important for binding to NUP133.[2] The yellow box and red vertical bars indicate the positions of added abnormal amino acids by the frameshift mutation and the positions of each point mutation, respectively.

Figure S14

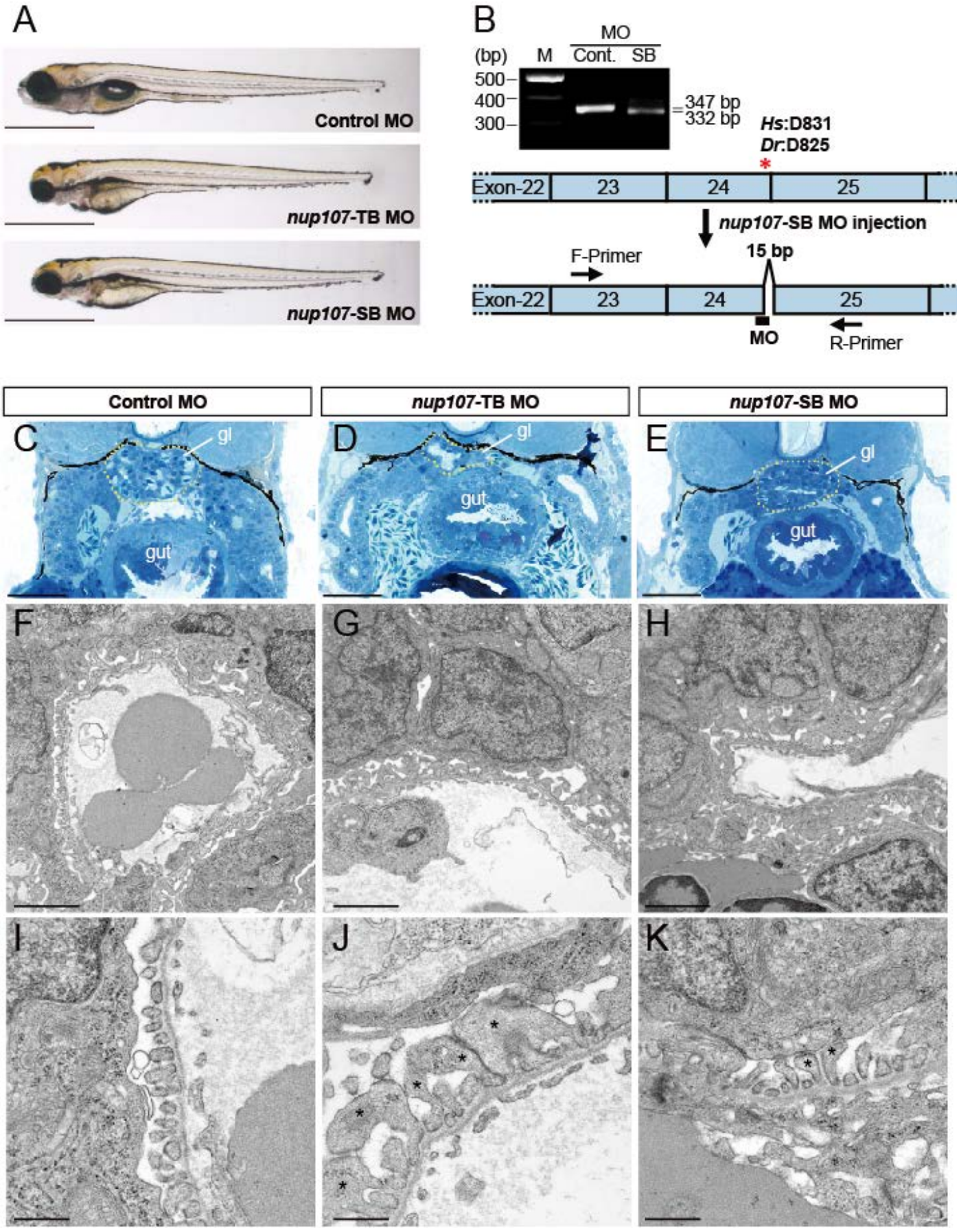

Figure S14. Zebrafish *nup107* Morphant Phenotype Recapitulates the Features of Human SRNS with

***NUP107* Mutations**

(A) Gross morphology of normal and affected larvae injected with control morpholino oligonucleotides (MO), *nup107* translation-blocking MO (*nup107*-TB MO) and *nup107* splice-blocking MO (*nup107*-SB MO). Lateral views of MO-injected larvae at 5 days post-fertilization (dpf) are shown. Scale bars: 1 mm. (B) RT-PCR sequencing of the aberrant splice products show a 15-bp in-frame deletion (WT; 347 bp, *nup107*-SB MO; 332 bp) in the coding exon included a five-amino-acid sequence conserved between humans and zebrafish. The conserved position of the substituted residue in affected individuals (*Homo sapiens*; p.Asp831, *Danio rerio*; p.Asp825) is shown as a red asterisk. The corresponding positions of the F-Primer, R-Primer, and MO are schematically presented. (C-E) Transverse sections of the glomerulus (gl) in the control MO-, *nup107*-TB MO- and *nup107*-SB MO-injected larvae at 5.5 dpf. Scale bars: 0.05 mm. (C) The control MO-injected larvae had a complete glomerular capillary and mesangium. (D) Morphology of the glomerulus and mesangium was markedly disrupted in the *nup107*-TB morphants. (E) The *nup107*-SB morphants showed hypoplastic glomerulus. (F–H) Electron micrographs of the MO-injected larvae at 5.5 dpf. Scale bars: 2 μm. (I–K) electron micrographs at higher magnification. Abnormal shape of the foot processes (asterisks), collapse of the capillary lumen and thickened basement membrane are seen in both *nup107*-TB and *nup107*-SB morphants (G, H, J, K), whereas the control morphant had a normal appearance (F, I). Scale bars: 500 nm.

Figure S15

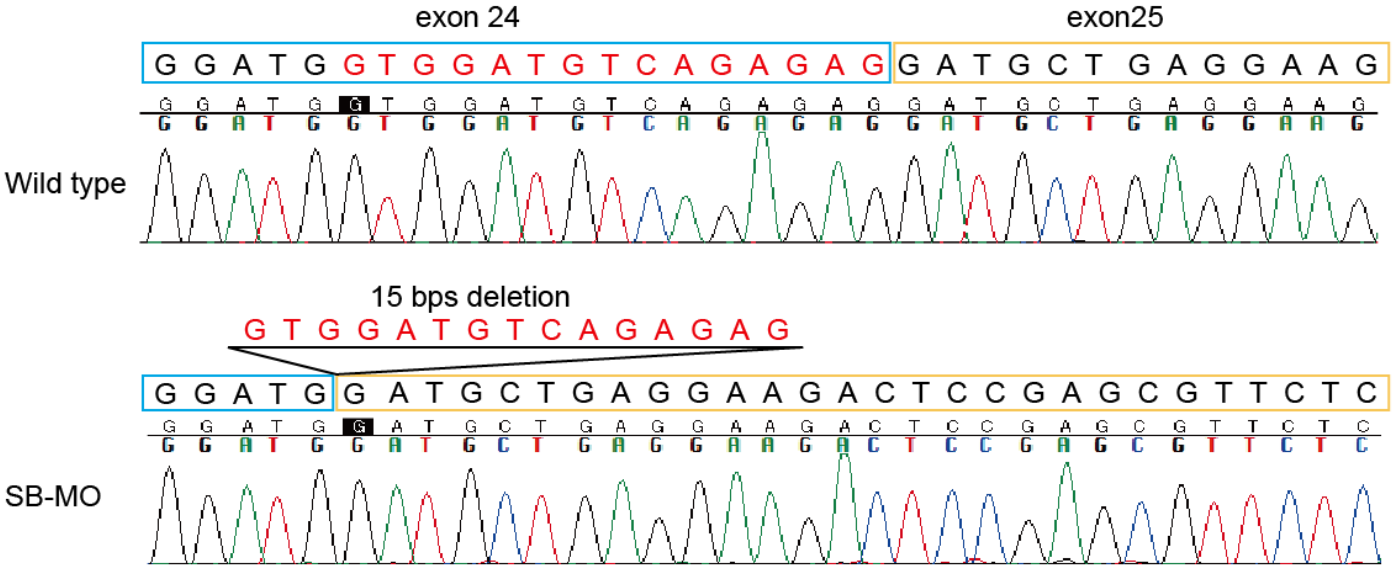

Figure S15. Chromatogram of cDNA sequences in wild-type and SB-MO zebrafish

cDNA sequence of SB-MO shows a 15-bp deletion (red characters) which resulted in an in-frame deletion.

Parts of exons 24 and 25 are indicated by light blue and orange boxes, respectively.

Figure S16

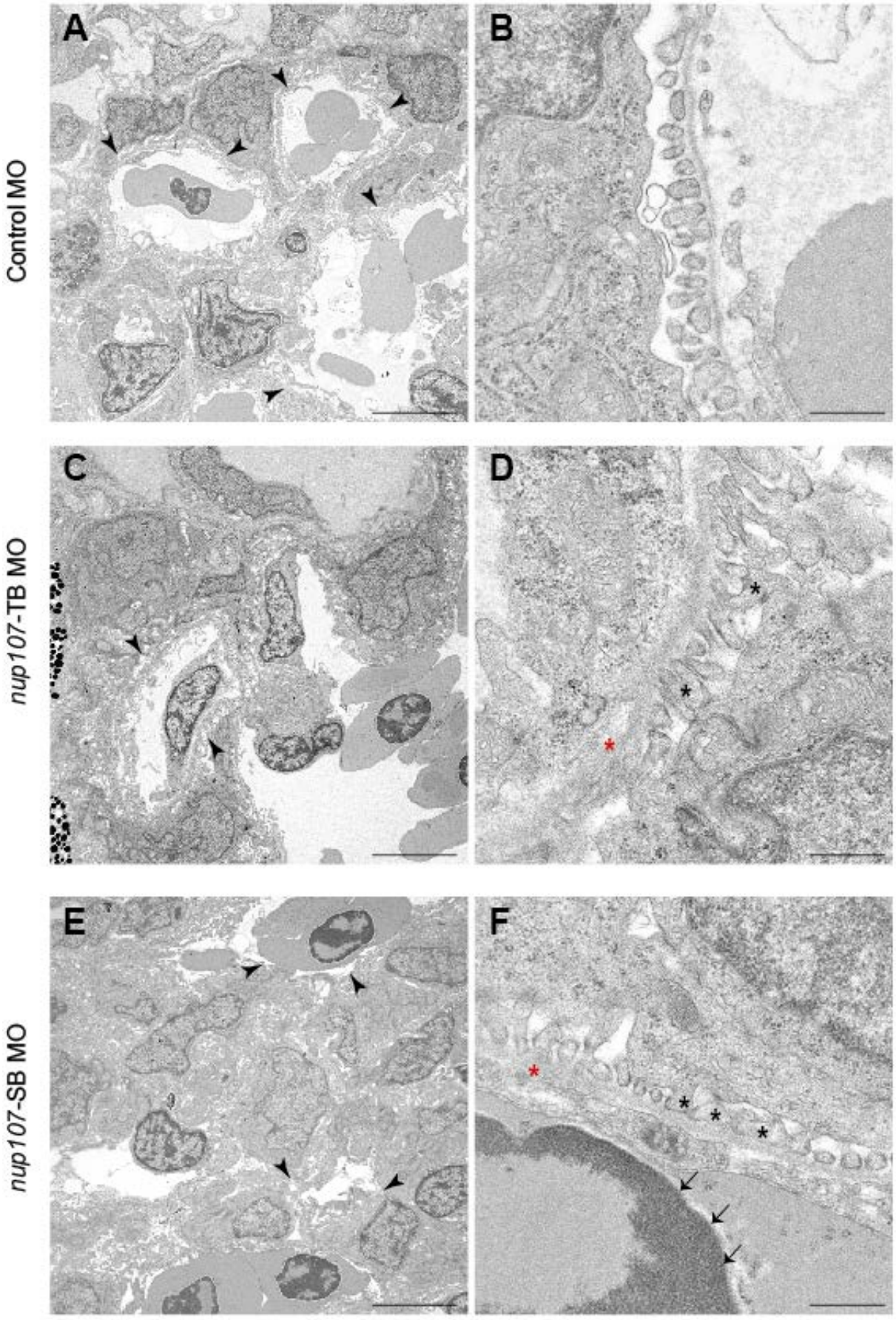

Figure S16. Electron Microscopy of Kidney Samples from Zebrafish *nup107*-Morphants

These electron micrographs depict tissue from the control morphant (A, B), the translation-blocking morphant (*nup107*-TB MO) (C, D), and the *nup107* splice-blocking morphant (*nup107*-SB MO) (E, F). The filtration structures (arrowheads) can be clearly observed in the control morphant (A) but are relatively fuzzy and disorganized in both of the other morphants (C, E). Abnormal foot processes (black asterisks), thickened or blurry basement membranes (red asterisks), and protein droplets (black arrows) could reflect cellular damage in the filtration apparatus. Scale bars: 5 μm (A, C, E); 500 nm (B, D, F).

Figure S17

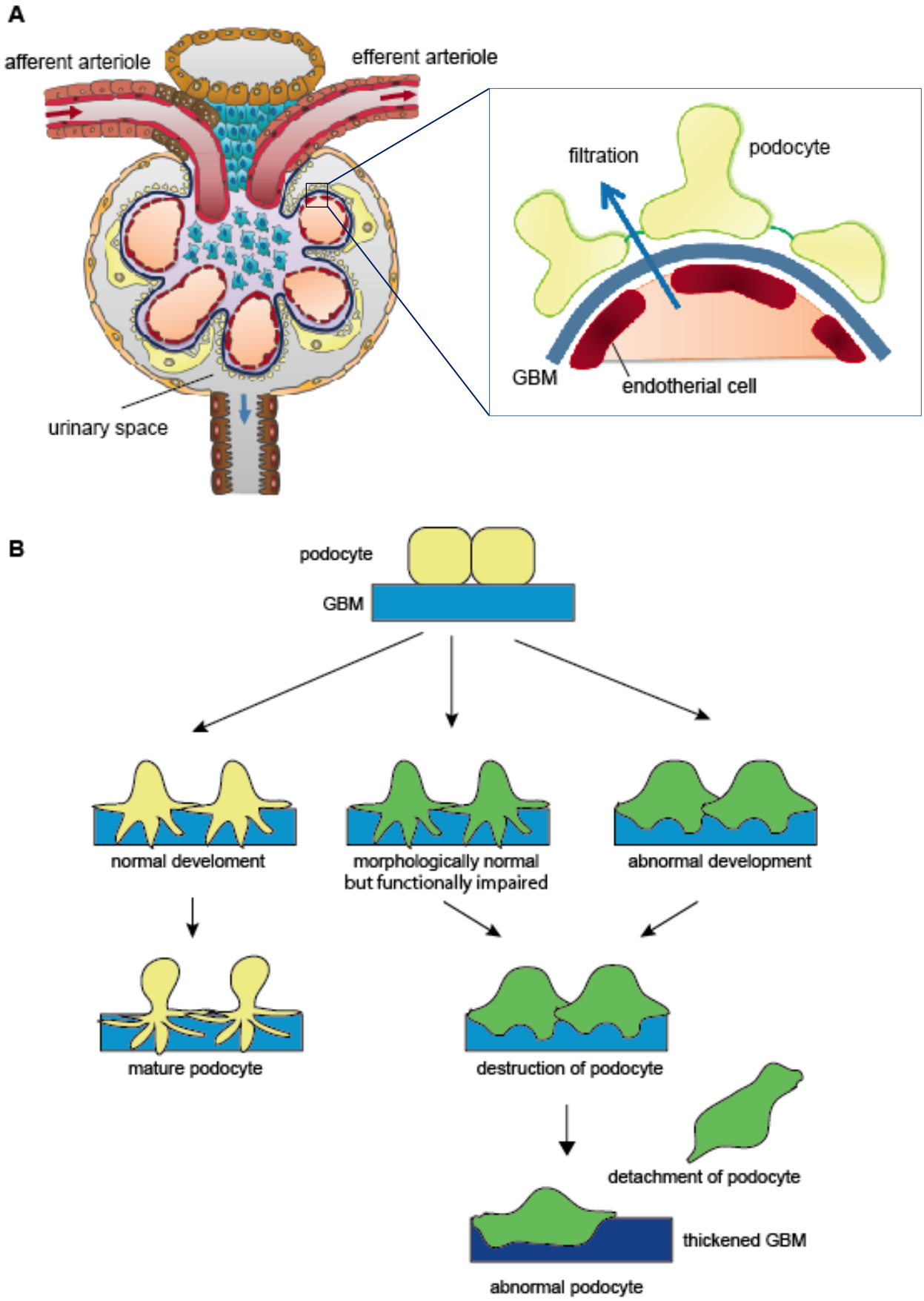

Figure S17. Podocyte Injury Model Based on *NUP107* Mutations

(A) Schematic presentation of the glomerulus. Podocytes (yellow) cover the outer layer of the capillary wall by projecting enormous foot processes with the glomerular basement membrane (dark blue). The inner surface of the capillary lumen is lined with endothelial cells (dark red). The capillary tuft is supported by mesangial cells (light blue) and surrounding matrix (light purple). The enlarged window shows the renal filtration structure. The foot processes of neighboring podocytes (yellow) connect with each other in an interdigitating fashion, leaving 20–50 nm intercellular filtration slits that are bridged by a specialized cell–cell junction known as the slit diaphragm (green line). The slit diaphragm serves as a filtration barrier, which prevents leakage of circulating proteins into the urine. Properly functioning podocytes are crucial for maintaining the integrity and selectivity of the barrier. (B) Podocytes first develop as attached columnar epithelial cells. Attachments between the podocyte cell bodies begin to separate except for the basal part that later forms foot processes through maturation.[3] Normal podocytes (yellow) interact with each other by their foot processes or with the slit membrane, and function as a filter. However, the abnormally developed podocytes (green) possess abnormally fragile foot processes (either by structure or function). As blood pressure increases after birth, the podocytes cannot withstand the post-natal capillary pressure and may become damaged. GBM: glomerular basement membrane.

Table S1. Summary of WES performance (read depth)

Family ID	Individual ID	Identification	Total (bps)	Mean depth	% ≥ 5×	% ≥ 10×	% ≥ 20×
SRNS-1	I-1	Father	2692208251	80.43	97.1	95.8	91.4
SRNS-1	I-2	Mother	2155302585	64.39	96.8	95	88.9
SRNS-1	II-4	Affected individual	2976332475	88.92	97.2	96.1	92.5
SRNS-2	I-2	Mother	1963459760	58.66	96.7	94.6	87.3
SRNS-2	II-1	Affected individual	2941457991	87.88	97.1	95.9	92.3
SRNS-TK1	I-1	Father	2799991123	83.65	97.1	95.8	91.8
SRNS-TK1	I-2	Mother	2322428088	69.38	96.9	95.3	89.9
SRNS-TK1	II-1	Affected individual	3081605879	92.06	97.2	96.2	92.9
SRNS-TWH1	I-1	Father	2506420047	74.88	96.9	95.4	90.4
SRNS-TWH1	I-2	Mother	2930587186	87.55	97	95.8	92.2
SRNS-TWH1	II-1	Affected individual	2698525857	80.62	97	95.7	91.6
SRNS-12	II-3	Affected individual	3210918988	95.93	96.9	95.6	92

Table S2. Priority scheme of homozygous variants in SRNS with *NUP107* mutations

	SRNS-1	SRNS-2	SRNS-TK1	SRNS-TWH1	SRNS-12
Homozygous in affected person as autosome	1139	1111	1136	1103	1120
Non-homozygous in father	153	NA	144	128	NA
Non-homozygous in mother	72	118	75	73	NA
Frequency of ≤ 0.005 in ExAC	19	19	19	19	75
Frequency of ≤ 0.005 in ESP6500	18	19	18	18	68
Frequency of ≤ 0.005 in HGVD	9	8	9	5	47
Frequency of ≤ 0.005 in in-house database	2	1	0	0	0
Non synonymous	1*	0	0	0	0

*The candidate homozygous mutation was listed in Table S4.

Table S3. Priority scheme of compound heterozygous variants in SRNS with *NUP107* mutations

	SRNS-1	SRNS-2	SRNS-TK1	SRNS-TWH1	SRNS-12
Heterozygous variants in affected person as autosome	2343	2146	2047	2089	1903
Non-homozygous in father	2255	NA	1964	1969	NA
Non-homozygous in mother	2144	2059	1861	1890	NA
Frequency of ≤ 0.005 in ExAC	1250	1164	1040	1133	1135
Frequency of ≤ 0.005 in ESP6500	1242	1156	1032	1124	1126
Frequency of ≤ 0.005 in HGVD	680	689	511	561	632
Frequency of ≤ 0.005 in In-house database	412	483	337	374	415
Non synonymous	285	350	229	237	288
Two or more variants in one gene	22	32*	24	20	18*
Compound heterozygous variant (gene)	8 (4)*	NA	6 (3)*	10 (4) *	NA

*The candidates for compound heterozygous variants are listed in Table S5. NA: not analyzed by WES.

Table S6. Mutant Genes Detected in SRNS/FSGS

Gene name	Accession number	MIM	Protein category
ACTN4	NM_004924.4	*604638	Actin cytoskeleton component
ADCK4	NM_024876.3	*615567	Related to CoQ10 synthesis
ANLN	NM_018685.2	*616027	Actin binding protein
APOL1	NM_003661.3	*603743	Secreted high density lipoprotein
ARHGAP24	NM_001025616.2	*610586	RHO GTPase-activating protein
ARHGDIA	NM_001185077.1	*601925	RHO GTPases
CAPN12	NM_144691.3	*608839	Cytosolic calcium-activated cysteine proteases
CD2AP	NM_012120.2	*604241	Slit-Diaphragm protein complex
CFH	NM_000186.3	*134370	Complement factor H
COL4A3	NM_000091.4	*120070	Collagen
COQ2	NM_015697.7	*609825	Mitochondrial protein
INF2	NM_022489.3	*610982	Filament network
LAMA5	NM_005560.3	*601033	Laminin
LAMB2	NM_002292.3	*150325	Glomerular basement membrane
LMNA	NM_170707.3	*150330	Lamin
LMX1B	NM_002316.3	*602575	Nuclear protein
MYH9	NM_002473.4	*160775	Actin cytoskeleton component
MYO1E	NM_004998.3	*601479	Myosin
NPHS1	NM_004646.3	*602716	Slit-Diaphragm protein complex
NPHS2	NM_014625.2	*604766	Slit-Diaphragm protein complex
NXF5	NM_032946.2	*300319	Nuclear RNA export factor 5
PAX2	NM_003987.3	*167409	Transcription factor
PLCE1	NM_016341.3	*608414	Slit-Diaphragm protein complex
PTPRO	NM_030667.2	*600579	Tyrosine phosphatase
SMARCAL1	NM_014140.3	*606622	Nuclear protein
TRPC6	NM_004621.5	*603652	Slit-Diaphragm protein complex
WT1	NM_024426.4	*607102	Nuclear protein

Supplemental References

1. Kitamura, A., Tsukaguchi, H., Iijima, K., Araki, J., Hattori, M., Ikeda, M., Honda, M., Nozu, K., Nakazato, H., Yoshikawa, N., et al. (2006). Genetics and clinical features of 15 Asian families with steroid-resistant nephrotic syndrome. Nephrol Dial Transplant 21, 3133-3138.

2. Boehmer, T., Jeudy, S., Berke, I.C., Schwartz, T.U. (2008). Structural and functional studies of Nup107/Nup133 interaction and its implications for the architecture of the nuclear pore complex. Mol Cell 30, 721-731.

3. Quaggin, S.E., Kreidberg, J.A. (2008). Development of the renal glomerulus: good neighbors and good fences. Development 135, 609-620.